

F. M. Mahafugur Rahman

## **Converter-side inductor design for a grid-connected converter equipped with an LCL filter**

**School of Electrical Engineering**

Thesis submitted for examination for the degree of Master of Science in Technology.

Esboo 14.03.2016

**Thesis supervisor:**

Prof. Marko Hinkkanen

**Thesis advisors:**

Jussi Koppinen, M.Sc. (Tech.)

Paavo Rasilo, D.Sc. (Tech.)

|   |                   |                        |
|---|-------------------|------------------------|
| Author: F. M. Mahafugur Rahman  |                   |                        |
| Title: Converter-side inductor design for a grid-connected converter equipped with an LCL filter  |                   |                        |
| Date: 14.03.2016  | Language: English | Number of pages: 10+61 |
| Department of electrical engineering  |                   |                        |
| Professorship: Electric Drives  |                   | Code: S-81             |
| Supervisor: Prof. Marko Hinkkanen   |                   |                        |
| Advisors: Jussi Koppinen, M.Sc. (Tech.), Paavo Rasilo, D.Sc. (Tech.)  |                   |                        |
| <p>An LCL filter is used between the grid and the grid converter to attenuate the switching harmonics. The LCL filter is one of the bulkiest and heaviest components in the grid-connected converter. The size of the LCL filter can be decreased significantly using higher switching frequencies enabled by next generation semiconductors. Further size reduction can be achieved using air-forced cooling conditions. This thesis presents the compact design of a converter-side inductor of an LCL filter. The design is implemented using the area product approach. The core material of the inductor is selected based on the highest peak flux density within saturation and core-loss density limits. Both the fundamental and the high frequency effects are considered to calculate the peak flux density. The winding wire is selected based on the rms current density. The gapped core is considered for the design and the effect of fringing flux on the inductance is studied. The thermal modeling of the inductor is included in the design. The design method is implemented on three different designs. The natural and the air-forced cooling conditions are considered. The effects of the peak flux density of the material and the effects of the cooling conditions on the size of the inductors are studied. A prototype inductor of <math>350 \mu\text{H}</math> is manufactured to verify the design algorithm. The 2605SA1 core material is used in the prototype inductor under air-forced cooling condition. Analytical and experimental results are presented.</p> |                   |                        |
| Keywords: Area product, cooling, fringing flux, grid converter, harmonic attenuation, inductor design, LCL filter, magnetic saturation, peak flux density, reluctance model, switching frequency  |                   |                        |

# Preface

First of all, thanks to Almighty Allah for the strength, guidance, and his abundant grace. The research work reported in this Master's thesis has been completed at Aalto University School of Electrical Engineering under the supervision of Prof. Marko Hinkkanen.

I would like to express my deepest gratitude to my supervisor for giving me the wonderful opportunity to conduct this thesis. I would like to thank him for his advice, guidance, and valuable suggestions regarding my thesis. I also want to thank my instructors Dr. Paavo Rasilo and specially to Jussi Koppinen for their comments, suggestions, and corrections in scientific writing. I would like to thank Waqar Ahmed Khan and Jukka Luomala for their comments and help throughout the thesis. I would like to thank all of my colleagues at electric drives research group for creating a pleasant working environment. I would like to thank my friends for their guidance.

Finally, I would like to express my deepest love and gratitude to my whole family, especially to my parents for their endless support and encouragement throughout my life.

Espoo, 14.03.2016

F. M. Mahafugur Rahman

# Contents

|  |     |
|--|-----|
| <b>Abstract</b>  | ii  |
| <b>Preface</b>   | iii |
| <b>Symbols and abbreviations</b>                       | vi  |
| <b>1 Introduction</b>                                  | 1   |
| <b>2 Grid converter with an LCL filter</b>             | 5   |
| 2.1 Grid-converter model . . . . .                     | 5   |
| 2.2 LCL-filter model . . . . .                         | 5   |
| 2.3 LCL-filter design . . . . .                        | 7   |
| 2.3.1 Design constraints . . . . .                     | 7   |
| 2.3.2 Optimization . . . . .                           | 8   |
| 2.3.3 Optimized parameters . . . . .                   | 8   |
| 2.4 Converter-side inductor design . . . . .           | 8   |
| <b>3 Fundamentals of magnetic theory</b>               | 10  |
| 3.1 Electromagnetic laws and relationships . . . . .   | 10  |
| 3.2 Magnetic circuits . . . . .                        | 12  |
| 3.2.1 Reluctance . . . . .                             | 13  |
| 3.2.2 Magnetic flux continuity . . . . .               | 13  |
| 3.3 Inductance . . . . .                               | 14  |
| 3.4 Magnetic hysteresis . . . . .                      | 15  |
| 3.5 Air-gap in magnetic core . . . . .                 | 16  |
| 3.6 Fringing flux . . . . .                            | 18  |
| 3.7 Losses in magnetic components . . . . .            | 19  |
| <b>4 Design of an inductor</b>                         | 21  |
| 4.1 Area product method . . . . .                      | 21  |
| 4.2 Inductor design algorithm . . . . .                | 21  |
| 4.3 Magnetic material . . . . .                        | 24  |
| 4.3.1 Magnetic material properties . . . . .           | 24  |
| 4.3.2 Magnetic material selection . . . . .            | 25  |
| 4.3.3 Peak flux density calculation . . . . .          | 27  |
| 4.4 Winding wire selection . . . . .                   | 27  |
| 4.4.1 Maximum current density . . . . .                | 27  |
| 4.4.2 Conductor selection . . . . .                    | 28  |
| 4.5 Core geometry selection . . . . .                  | 28  |
| 4.6 Number of turns calculation . . . . .              | 29  |
| 4.7 Air-gap calculation . . . . .                      | 30  |
| 4.7.1 Magnetic circuit without fringing flux . . . . . | 30  |
| 4.7.2 Magnetic circuit with fringing flux . . . . .    | 31  |

|                   |   |           |
|-------------------|---|-----------|
| 4.8               | Winding arrangements . . . . .                                  | 33        |
| 4.9               | Loss calculation . . . . .                                      | 34        |
| 4.9.1             | Winding loss . . . . .  | 34        |
| 4.9.2             | Core loss . . . . .   | 35        |
| 4.9.3             | Air-gap loss . . . . .  | 36        |
| 4.9.4             | Total power loss . . . . .                                      | 37        |
| 4.10              | Thermal modeling . . . . .                                      | 37        |
| <b>5</b>          | <b>Results</b>  | <b>40</b> |
| 5.1               | Design examples . . . . .                                       | 40        |
| 5.1.1             | Design example 1: Natural cooling (Amorphous core) . . . . .    | 41        |
| 5.1.2             | Design example 2: Air-forced cooling (Amorphous core) . . . . . | 41        |
| 5.1.3             | Design example 3: Air-forced cooling (JNHF core) . . . . .      | 42        |
| 5.1.4             | Discussion . . . . .  | 43        |
| 5.2               | Experiments . . . . .   | 45        |
| <b>6</b>          | <b>Conclusions</b>  | <b>51</b> |
| <b>References</b> |   | <b>53</b> |
| <b>Appendix</b>   |   | <b>57</b> |

# Symbols and abbreviations

## Symbols

Boldface letters represent the matrices and the vectors. The magnitude of the vectors are denoted by plain uppercase italic letters.

|                    |   |
|--------------------|---|
| $A$                | Width of the core                                     |
| $A_{\text{ag}}$    | Cross-section area of the air-gap                     |
| $A_c$              | Cross-section area of the core                        |
| $A_{\text{ca}}$    | Core open surface                                     |
| $A_{c,\text{eff}}$ | Effective cross-sectional area of the core            |
| $A_{\text{cv}}$    | Convecting area of the component                      |
| $A_o$              | Dowell's constant                                     |
| $A_p$              | Area product of the inductor                          |
| $A_{p,\text{cal}}$ | Calculated area product of the inductor               |
| $A_r$              | Radiating area of the component                       |
| $A_w$              | Area of the bare conductor                            |
| $A_{\text{wa}}$    | Conductor open surface                                |
| $A_{\text{wc}}$    | Conduction surface between the conductor and the core |
| $A_{\text{ws}}$    | Winding single turn cross-section area                |
| $A_{w,\text{tot}}$ | Winding total cross-section area                      |
| $B$                | Width of the window                                   |
| $B_{\text{pk}}$    | Peak flux density                                     |
| $B_r$              | Remanence flux density                                |
| $B_{\text{sat}}$   | Saturation flux density                               |
| $B_{\text{sw,pk}}$ | Peak flux density due to the ripple current           |
| $B_{1,\text{pk}}$  | Peak flux density due to the fundamental current      |
| $C$                | Length of the core-window                             |
| $C_{\text{dc}}$    | Dc-link capacitor                                     |
| $C_f$              | Shunt capacitor                                       |
| $d$                | Conductor diameter                                    |
| $d_o$              | Nominal outer conductor diameter                      |
| $D$                | Height of the core                                    |
| $e(t)$             | Induced electromotive force                           |
| $\mathbf{E}$       | Electric field intensity                              |

|   |  |
|---|--|
| $f_{\text{sw}}$   | Switching frequency                                  |
| $F$   | Length of the core                                   |
| $F_f$   | Fringing flux factor                                 |
| $F_R$   | Winding ac-to-dc resistance ratio                    |
| $\mathcal{F}$   | Magnetomotive force                                  |
| $h_c$   | Convection heat transfer coefficient of the material |
| $h_i$   | Height of the inductor                               |
| $H, \mathbf{H}$   | Magnetic field intensity                             |
| $H_b$   | Height of the bobbin                                 |
| $H_{\text{co}}$   | Coercive field of the material                       |
| $H_t$   | Total length of the boundary layer of the component  |
| $H_v$   | Vertical height of the component                     |
| $i$   | Applied ac current                                   |
| $i_{\text{ca}}, i_{\text{cb}}, i_{\text{cc}}, \mathbf{i}_c$ | Converter-side currents                              |
| $i_E$   | Induced eddy current                                 |
| $\mathbf{i}_g$  | Grid-side current                                    |
| $I_{\text{pk}}$   | Peak value of the current                            |
| $I_{\text{rms}}$  | Rated rms current                                    |
| $I_{\text{rp}}$   | Converter ripple current                             |
| $I_{\text{sc}}$   | Maximum short-circuit current                        |
| $I_{\text{sw,pk-pk}}$                                       | Peak-to-peak ripple current                          |
| $I_{1,\text{pk}}$   | Peak value of the fundamental current                |
| $J_m$   | Rms current density                                  |
| $k$   | Steinmetz's equation parameter                       |
| $k_c$   | Core fill factor                                     |
| $k_i$   | Core constant  |
| $k_{\text{ta}}$   | Thermal conductivity of air                          |
| $k_{\text{tc}}$   | Thermal conductivity of the core material            |
| $K_e$   | Eddy-current loss constant                           |
| $K_h$   | Hysteresis loss constant                             |
| $K_u$   | Window utilization factor                            |
| $l$   | Total length of the magnetic path                    |
| $l_{\text{ag}}$   | Length of each air-gap                               |
| $l_{\text{ag,t}}$   | Total length of air-gap                              |
| $l_c$   | Mean length of the magnetic core                     |
| $l_i$   | Length of inductor                                   |
| $l_{\text{T},1}$  | Winding length per single turn at the first layer    |

|                     |  |
|---------------------|--|
| $l_{T,2}$           | Winding length per single turn at the second layer                                   |
| $l_w$               | Total winding length   |
| $l_{wc}$            | Equivalent air-gap corresponding to the air space between the conductor and the core |
| $L$                 | Inductance   |
| $L_{\text{cal}}$    | Calculated inductance  |
| $L_{\text{fc}}$     | Converter-side inductance  |
| $L_{\text{fg}}$     | Grid-side inductance   |
| $m_c$               | Mass of the core   |
| $m_i$               | Mass of the inductor   |
| $n$                 | Harmonic number  |
| $N$                 | Number of turns  |
| $N_l$               | Number of winding layers   |
| $N_{\max}$          | Maximum number of fitted turns in the core   |
| $N_{tl}$            | Number of turns per layer  |
| $N_{tl,1}$          | Number of turns at the first layer   |
| $N_{tl,2}$          | Number of turns at the second layer  |
| $p$                 | Distance between the centres of two adjacent conductors                              |
| $p_v$               | Core loss density  |
| $P_{\text{ag}}$     | Air-gap loss   |
| $P_c$               | Total core loss  |
| $P_h$               | Power loss due to the hysteresis effect  |
| $P_e$               | Eddy current loss  |
| $P_{\max}$          | Maximum power loss margin  |
| $P_t$               | Total power loss   |
| $P_w$               | Winding total loss   |
| $P_{w(\text{dc})}$  | Winding loss due to dc resistance  |
| $q$                 | Total heat transfer rate   |
| $q_{cd}$            | Conduction heat transfer rate  |
| $q_{cv}$            | Convection heat transfer rate  |
| $q_r$               | Radiation heat transfer rate   |
| $R_{ca}$            | Thermal resistance between the core and the ambient                                  |
| $R_{ca, \text{cv}}$ | Convection thermal resistance between the core and the ambient                       |
| $R_{ca,r}$          | Radiation thermal resistance between the core and the ambient                        |
| $R_{\text{fc}}$     | Equivalent series resistance on the converter-side                                   |
| $R_{\text{fg}}$     | Equivalent series resistance on the grid-side  |
| $R_{hs,w}$          | Conduction thermal resistance of the conductor                                       |
| $R_{\text{th}}$     | Total thermal resistance of the inductor   |

|                                  |  |
|----------------------------------|--|
| $R_{\text{wa}}$                  | Thermal resistance between the conductor and the ambient                 |
| $R_{\text{wa,cv}}$               | Convection thermal resistance between the conductor and the ambient      |
| $R_{\text{wa,r}}$                | Radiation thermal resistance between the conductor and the ambient       |
| $R_{\text{wc}}$                  | Thermal resistance between the conductor surface and the core            |
| $R_{\text{wc,cd}}$               | Conduction thermal resistance between the conductor surface and the core |
| $R_{\text{wc,r}}$                | Radiation thermal resistance between the conductor surface and the core  |
| $R_{\text{w(ac)}}$               | Total winding resistance   |
| $R_{\text{w(dc)}}$               | Winding dc resistance  |
| $\mathcal{R}_{\text{ag}}$        | Reluctance of the air-gap  |
| $\mathcal{R}_c$                  | Reluctance of the core   |
| $\mathcal{R}_{\text{eq}}$        | Total equivalent reluctance  |
| $\mathcal{R}_{\text{eq,f}}$      | Equivalent reluctance with the fringing effect                           |
| $\mathcal{R}_f$                  | Reluctance of the fringing flux  |
| $T_a$                            | Ambient temperature  |
| $T_c$                            | Temperature of the core surface  |
| $T_{\text{hs}}$                  | Temperature of the hot-spot  |
| $T_{\max}$                       | Maximum temperature margin   |
| $T_w$                            | Temperature of the the conductor surface                                 |
| $\mathbf{u}_c$                   | Converter-side voltage   |
| $u_{\text{dc}}$                  | Dc-link voltage  |
| $\mathbf{u}_f$                   | Capacitor voltage  |
| $u_{\text{gab}}, u_{\text{gbc}}$ | Line-to-line grid voltages   |
| $\mathbf{u}_g$                   | Grid-side voltage  |
| $v$                              | Velocity of the air  |
| $V_c$                            | Volume of the magnetic core  |
| $V_i$                            | Volume of the inductor   |
| $V_w$                            | Volume of the winding  |
| $w_h$                            | Energy loss density of the core  |
| $w_i$                            | Width of the inductor  |
| $w_l$                            | Lamination width   |
| $W_a$                            | Window area of the core  |
| $W_{\text{cycle}}$               | Energy loss over one cycle   |
| $W_L$                            | Stored energy of the inductor  |

|                    |  |
|--------------------|--|
| $\alpha, \beta$    | Steinmetz's equation parameters                        |
| $\delta_w$         | Skin depth of the conductor                            |
| $\varepsilon_c$    | Emissivity of the core surface                         |
| $\varepsilon_w$    | Emissivity of the conductor surface                    |
| $\mu_0$            | Permeability of the free space                         |
| $\mu_{\text{eff}}$ | Relative permeability of the material with gapped core |
| $\mu_r$            | Relative permeability of the material                  |
| $\mu_{rw}$         | Winding relative permeability                          |
| $\rho_w$           | Electrical resistivity of the copper wire              |
| $\sigma$           | The Stefan-Boltzmann constant                          |
| $\phi$             | Magnetic flux  |
| $\phi_{\text{ag}}$ | Magnetic flux in the air-gap                           |
| $\phi_c$           | Magnetic flux in the core                              |
| $\phi_f$           | Fringing flux  |
| $\psi$             | Magnetic flux linkage                                  |
| $\Delta T$         | Temperature rise in the inductor                       |

## Abbreviations

|                    |  |
|--------------------|--|
| FRA                | Frequency response analyzer                      |
| GaN                | Gallium nitride                                  |
| iGSE               | Improved generalized Steinmetz equation          |
| i <sup>2</sup> GSE | Improved-improved generalized Steinmetz equation |
| MMF                | Magnetomotive force                              |
| MSE                | Modified Steinmetz equation                      |
| PWM                | Pulse-width modulation                           |
| SCR                | Short circuit ratio                              |
| SE                 | Steinmetz equation                               |
| SiC                | Silicon carbide                                  |
| SVPWM              | Space-vector pulse-width modulation              |
| THD                | Total harmonic distortion                        |
| VSC                | Voltage source converter                         |

# 1 Introduction

High energy prices and environmental concerns are driving the search for distributed resources and distributed generations. Providing electricity to serve remote areas is a challenge for existing electricity distribution networks. The rising cost and complexity in existing electricity distribution networks have led to a search for alternative distribution methods. The targets of the distribution network are reducing the transmission and distribution losses and improved reliability of the power supply. Many of the distributed resources use renewable energies such as wind and solar [1, 2]. Electrical energy in the form of dc can be generated from photovoltaic and fuel cells. On the other hand, some of the distributed resources provide electricity in the form of ac.

The connection of a dc voltage source to the utility grid needs a dc/ac conversion stage. In case of distributed ac sources, it is preferred to perform energy exchange through an ac/dc/ac conversion stage for synchronization of the generated voltage and frequency with the utility grid [2]. There is a high demand for active front-end two level grid converters to interface between the utility grid and the various sources. The most commonly used power converter is a pulse-width modulation (PWM) voltage source converter (VSC) [1,3–5]. A characteristic of the conventional semiconductors used in voltage source converters is that their switching frequency is limited to 4-8 kHz. Consequently, the converter output voltage contains significant harmonics at the switching frequency [6]. To ensure a good quality of the grid voltage, the switching harmonics generated by the grid-converter should be attenuated to an acceptable level given by grid standards such as IEEE 519-2014 [7].

A low-pass power filter is often inserted between the VSC and the utility grid to attenuate harmonic currents generated by PWM to the desirable limits. The simplest structure is to use an inductor between the VSC and the utility grid [3, 4]. It has the least number of components but only 20 dB per decade attenuation. A large inductance value is needed to meet the grid standards. A third-order LCL filter structure is the most widely used structure [3, 4, 8–10]. The LCL filter has 60 dB per decade attenuation at high frequencies. Thus, the LCL filter can meet the same filtering performance with smaller overall inductance value. However, due to

the resonance, controlling might be more difficult to keep the system stable. Furthermore, selecting the parameters of an LCL filter is a more complicated process in comparison with the traditional L filters. The LLCL filter in [5] can attenuate the switching-frequency current ripple components better than the LCL filter, but requires an extra component.

In the grid-connected converter, the LCL filter is one of the bulkiest and heaviest components. Furthermore, considerable losses occur in these magnetic components. As the power rating increases, the size of the LCL filter increases. In the case of multi-megawatt VSC, the weight of the LCL filter can reach hundreds of kilograms as well as the cost of the filter increases [4]. Thus, the weight reduction of the LCL filter is an even greater concern. The reduction of size and weight of the LCL filter can be driven by cost considerations, space availability and increasing efficiency requirements. One typical method to achieve a compact size of the LCL is to minimize the stored energy of the magnetic components at the rated operating point without exceeding the grid-current harmonic limits. The increase of the power density of any equipment always affects the efficiency: a trade-off between volume and losses has to be made [9]. When keeping the volume constant, lower losses occur in the inductive components. In order to increase the power density, losses in the inductors must be reduced.

Switching circuits, operating at high frequencies have led to substantial reductions in size of inductive components [11, 12]. Recent developments in power semiconductor devices have improved in terms of higher current or voltage ratings. Furthermore, lower switching and conduction losses are allowing higher switching frequencies in the converters. The next generation semiconductors based on wide band-gap materials, such as silicon carbide (SiC) and gallium nitride (GaN) devices, can switch with a much higher frequency than the silicon (Si) device does without causing more switching losses [5]. Wide band-gap devices have resulted in a significant improvement of the operating-voltage range for unipolar devices and of the switching speed compared with Si power devices [13]. The freedom of increasing the switching frequency is advantageous for a grid converter also, since it allows reducing the size of the inductors of the LCL filter. Thus, the wide band-gap devices give us the possibility to design a more compact LCL filter.

However, if higher switching frequencies are applied, the high frequency behaviour of the inductor has to be taken into consideration. This gives us possibility to achieve higher accuracy in meeting the existing grid standards. The equivalent resistance of the inductor increases and the equivalent inductance decreases with frequency due to the skin and proximity effects [14]. Moreover, the winding ac resistance in the inductor depends on the length of the winding and also the skin and proximity effects which increase with number of turns and layers in the coil winding [15, 16]. These frequency-dependent phenomena reduce the filtering capability of the LCL filter due to the lower inductance at higher frequencies. Further, the damping ratio of the resonance is increased due to the higher resistivity at higher frequencies. In

addition, the resistance and the inductance of the inductor are material depended. Aforementioned aspects can be considered in designing an inductor for an LCL filter connected to the grid converter.

There are several kinds of inductor design procedures. The designs involve the steps: core material selection, core shape and size, and winding wire selection [17,18]. Usually, the core material is selected before starting the design. However, the selection of the core material for the design is not straightforward [19]. The area product and the core geometry method are well-known strategies for selecting the core shape and size [17]. The area product is defined by the product between the core window area and the core cross-sectional area. The concept of the area product design approach is to select a proper core satisfying both the electromagnetic conditions and the restriction of the core window area [20]. During the design process, the area product value is calculated numerically using the magnetic and electric properties of the inductor. Further, the area product value is computed from manufacturers technical data-sheet about the core material. However, the core is selected based on the obtained area product value using data-sheet that is about 10% higher than the calculated area product value [18].

Magnetic components are optimized using the area product approach in [11,12,17,18, 20, 21]. Solid single wire winding, optimum strand diameter winding, and multiple-strand winding configurations using the area product approach are explained in [17]. High-frequency skin and proximity effects are considered in formulation of winding losses in [12, 20]. A comparative study of pre-optimized linear and non-linear inductors using the area-product formulation is presented in [21] for approximate size prediction. On the other hand, the concept of the core geometry approach is to select a proper core satisfying the electromagnetic conditions, the restriction of the core window area, and the restriction of the winding loss. This method is useful to design inductors when the copper and core losses are the dominant constraint [18, 22]. Designing of inductor using core geometry approach is presented in [17, 18, 22].

In [23], the LCL filter is optimized for a 12.5-kVA SiC grid converter using the switching frequency of 20 kHz. Thus, the converter current through the inductor has a fundamental component of 50 Hz and a superimposed ripple current of 20 kHz. Both the fundamental and high frequency effects are taken into account. During the optimization, the stored energy of the magnetic components in the filter is minimized. Parameter values are obtained based on the grid-current harmonic limits. The objective of this thesis is to design a compact converter-side inductor of an LCL filter connected to a grid converter. The design of the inductor is implemented using the area product approach. A minimum area product is the optimization target. The design of inductor is implemented by a single-wire winding with a gapped core taking into account the fringing effects.

This thesis explores the compact design of a converter-side inductor of an LCL filter which leads to optimized core selection, calculation of peak flux density and optimum wire diameter of the windings from the design specifications. The thesis

describes the mathematical background of the area product method along with example designs. Both the natural and air-forced cooling conditions are considered. Various core materials are considered and the design algorithms are implemented. Different design examples are compared. Once the physical properties of the core and winding are established, a prototype inductor of  $350 \mu\text{H}$  has been made using the amorphous core material under forced cooling condition. Furthermore, the phenomena of the prototype inductor are investigated by means of experiments.

The thesis consists of six sections. Section 2 introduces the grid-connected converter equipped with an LCL filter. It also describes the optimization of the LCL filter and gives the parameters of the grid-connected converter. Further, the interest behind the design of converter-side inductor is explained in section 2. Section 3 introduces briefly the fundamentals of the magnetic theory. In this section, a magnetic circuit model with the effect of the air-gap fringing flux is explained. Section 4 describes the design algorithm of the converter-side inductor using the area product method. Section 5 presents the simulations and the experimental results and compares the state of adjustment. Finally, section 6 gives an overview the results of the work, as well as the further research questions.

## 2 Grid converter with an LCL filter

This section presents the system modelling of a grid-connected converter equipped with an LCL filter. The LCL filter model is explained briefly with the equivalent circuit. This section describes briefly the LCL-filter design and the filter optimization. Finally, this section provides the optimized parameters.

### 2.1 Grid-converter model

A grid-connected converter converts electricity from a source with an ability of synchronization to interface with the utility grid. The active two-level grid-connected converters are widely used for grid connection of renewables and in ac drives for being able to feed braking energy back to the grid. Fig. 2.1 shows a grid-connected converter equipped with an LCL filter. In each phase, one pair of semiconductor switches allows the transfer of power. The switches are connected to the dc-link capacitor  $C_{dc}$ . The semiconductor switches are assumed to be ideal. The dc-link voltage is denoted by  $u_{dc}$ . The line-to-line grid voltages are denoted by  $u_{gab}$  and  $u_{gbc}$ , and the converter-side currents are denoted by  $i_{ca}$ ,  $i_{cb}$ , and  $i_{cc}$ . The output voltage of the converter contains unwanted switching harmonics generated by the PWM. An interface filter is needed to limit the current ripple and to attenuate the switching harmonics according to the grid standards. An attractive way to attenuate the switching harmonics is to use an LCL filter between the grid and the converter.

### 2.2 LCL-filter model

Fig. 2.2 shows the space-vector model of the three-phase LCL filter. The LCL filter is composed of the inductors with the equivalent series resistance  $R_{fc}$  and the inductance  $L_{fc}$  on the converter-side, the shunt capacitors  $C_f$ , and the inductors with the equivalent series resistance  $R_{fg}$  and the inductance  $L_{fg}$  on the grid-side. The capacitor resistance and the grid impedance are assumed to be zero for simplicity.

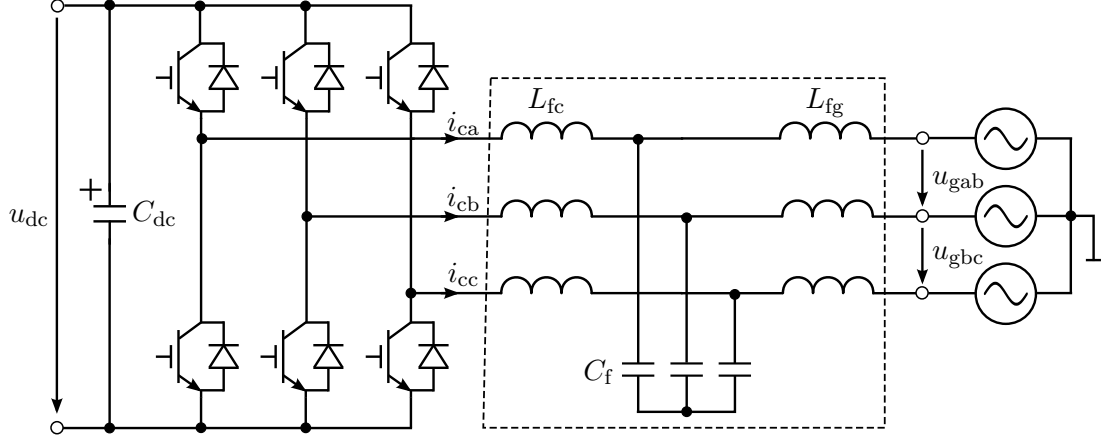


Figure 2.1: Grid-connected converter equipped with an LCL filter.

The converter-side voltage is denoted by  $\mathbf{u}_c$ , the capacitor voltage by  $\mathbf{u}_f$ , and the grid voltage by  $\mathbf{u}_g$ . The converter and grid-side currents are  $\mathbf{i}_c$  and  $\mathbf{i}_g$ , respectively.

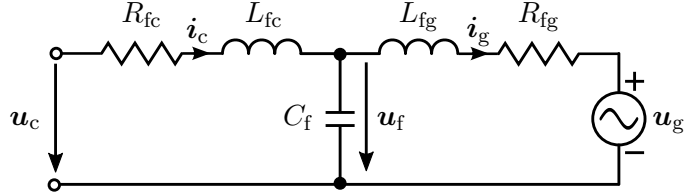


Figure 2.2: Equivalent circuit of an LCL filter.

Typically, the LCL filter is modelled using constant parameter values [3, 10, 24–26]. Since the losses in the filter are relatively small, particularly with higher power ratings, the influences of the equivalent series resistances are neglected. However, the equivalent series resistance increases and the inductance decreases with frequency due to skin and proximity effects. The combination of the equivalent series resistances contribute to damping.

In [23], the modified LCL filter model is presented. The skin and proximity effects stay negligible in the low core-loss material. Moreover, the low core-loss materials prevent overheating produced by the high converter-current ripple. Therefore, the constant-parameter model is used in [23] on the converter-side considering the low core-loss material. On the other hand, a laminated iron-core inductor is used on the grid-side due to low grid-current ripple. The frequency behaviour of the grid-side inductor is examined using a frequency-dependent lumped-parameter model. As seen from [23], the equivalent high-frequency core model is more accurate than the constant parameter model. The LCL filter model is evaluated by means of simulations. The grid-side inductor is modelled with two series-connected Foster elements. The parameter values of the Foster elements are obtained by fitting the frequency response of the Foster elements with the analytical response. Moreover, as

Table 2.1: Maximum odd harmonic current distortion in percent of rated current  $I_1$  for distribution systems (120 V - 69 kV) according to IEEE-519 [7].  $I_{sc}$  defines the maximum short-circuit current and  $n$  defines the harmonic number. Even harmonics are limited to 25% of the odd harmonics.

| $I_{sc}/I_1$ | $3 \leq  n  < 11$ | $11 \leq  n  < 17$ | $17 \leq  n  < 23$ | $23 \leq  n  < 35$ | $35 \leq  n  \leq 50$ | THD  |
|--------------|-------------------|--------------------|--------------------|--------------------|-----------------------|------|
| < 20         | 4.0               | 2.0                | 1.5                | 0.6                | 0.3                   | 5.0  |
| 20 < 50      | 7                 | 3.5                | 2.5                | 1.0                | 0.5                   | 8.0  |
| 50 < 100     | 10                | 4.5                | 4.0                | 1.5                | 0.7                   | 12.0 |
| 100 < 1000   | 12.0              | 5.5                | 5.0                | 2.0                | 1.0                   | 15.0 |
| > 1000       | 15.0              | 7.0                | 6.0                | 2.5                | 1.4                   | 20.0 |

can be seen from [23], the resonance is damped due to the high grid-side equivalent series resistance at high frequencies.

## 2.3 LCL-filter design

The LCL filter is designed for a 12.5 kVA, 50 Hz SiC grid converter using the switching frequency of 20 kHz. The design method considers the high-frequency behavior of the inductors as described in [23]. The rating of the converter is as follows: line-to-line rms voltage of 400 V, dc bus voltage of 650 V, and the rated current of 18.30 A. The converter voltage reference is calculated based on the desired fundamental grid current. The space-vector pulse-width modulation (SVPWM) method is used. The modulator is assumed to operate in the linear region. The harmonic components of the converter voltage are calculated numerically from the time-domain voltage waveforms. Then, the harmonic components of the converter voltage are determined by means of the discrete Fourier transform.

### 2.3.1 Design constraints

The LCL filter is designed to meet the harmonic distortion limits according to IEEE 519-2014. The harmonic distortion limits are shown in Table 2.1. The harmonic distortion limits vary for different values of short circuit ratio (SCR). The SCR less than 20 is assumed. When the SCR is below 20, the maximum allowed grid current harmonic is 0.3% of the rated current for the harmonic numbers higher than 35. The total harmonic distortion (THD) is kept below 5%. A conservative approach is considered for the optimization. The converter-current THD is set below 12% in order to limit the losses in the converter-side inductor and the converter. In the analysis, both the positive and negative sequences are considered.

### 2.3.2 Optimization

The size of the LCL filter decreases if the value of the inductances decrease. The values of inductances and capacitance of the LCL filter are varied to obtain the optimal design. The total area product of the LCL filter is proportional to the sum of the values of the converter-side inductance and the grid-side inductance. Therefore, the smaller values of the inductors provide a compact LCL filter. One typical method to achieve a compact LCL filter is to minimize the stored energy of the magnetic components in the filter at the rated operating point [6, 23]. Since, the inductor energy is proportional to the inductor area product, a compact size can be achieved.

### 2.3.3 Optimized parameters

The optimized parameter values are  $L_{fc} = 350 \mu\text{H}$ ,  $C_f = 10 \mu\text{F}$ , and  $L_{fg} = 250 \mu\text{H}$ . A conventional filter is used in [24] with a grid-connected converter having the switching frequency of 6 kHz. The filter parameter values are  $L_{fc} = 2.94 \text{ mH}$ ,  $C_f = 10 \mu\text{F}$ , and  $L_{fg} = 2.8 \text{ mH}$ . The total inductance of the optimized LCL filter is about 10% of the total inductance of the conventional filter used in [24]. The value of the capacitance is same as the conventional filter capacitor.

A grid converter was simulated by applying the optimized parameter values. Fig. 2.3 shows the simulated waveform of the converter current. The simulated grid current waveform is shown in Fig. 2.4. According to the results, the peak value of the converter current is  $I_{pk} = 28.12 \text{ A}$  and the converter ripple current is  $I_{rp} = 2.06 \text{ A}$ . The simulated peak-to-peak ripple current is  $I_{sw,pk-pk} = 4.67 \text{ A}$ .

## 2.4 Converter-side inductor design

The shunt capacitor impedance can be considered to be negligible at the frequencies at which significant harmonics exist [25]. At these frequencies, the rate of rise of the current is limited mainly by the impedance of the converter-side inductor. It is assumed that the peak value of the grid-current corresponds to the peak value of the fundamental current (cf. Fig. 2.4) when an LCL filter is used [6]. In contrast, the converter-current contains significant amount of ripple current. The peak value of the converter-current is composed of the peak value of the fundamental current and the peak value of ripple current [6]. The converter-side inductor has to endure high frequency ripple current (cf. Fig. 2.3). The high frequency current ripple causes more core losses in the converter-side inductor. Thus, the ripple current has a great impact on the choice of the core material and the dimension of the core in order to avoid magnetic saturation and to dissipate the heat to avoid excessive temperature rise. In contrast, the grid-side inductor has lower loss in comparison with the converter-side inductor. Thus, the converter-side inductor is typically a more expensive component than the grid-side inductor. The converter-side inductor

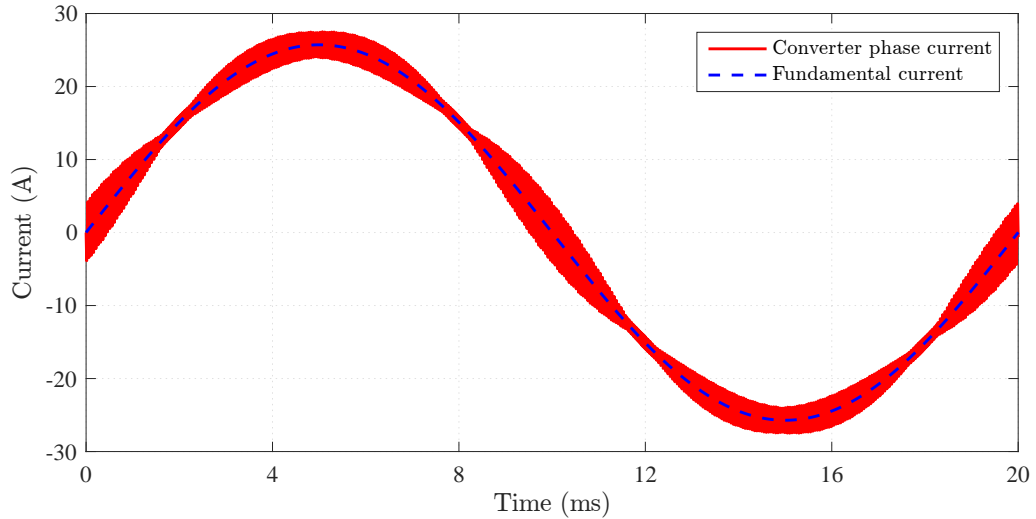


Figure 2.3: Simulated waveform of the converter current.

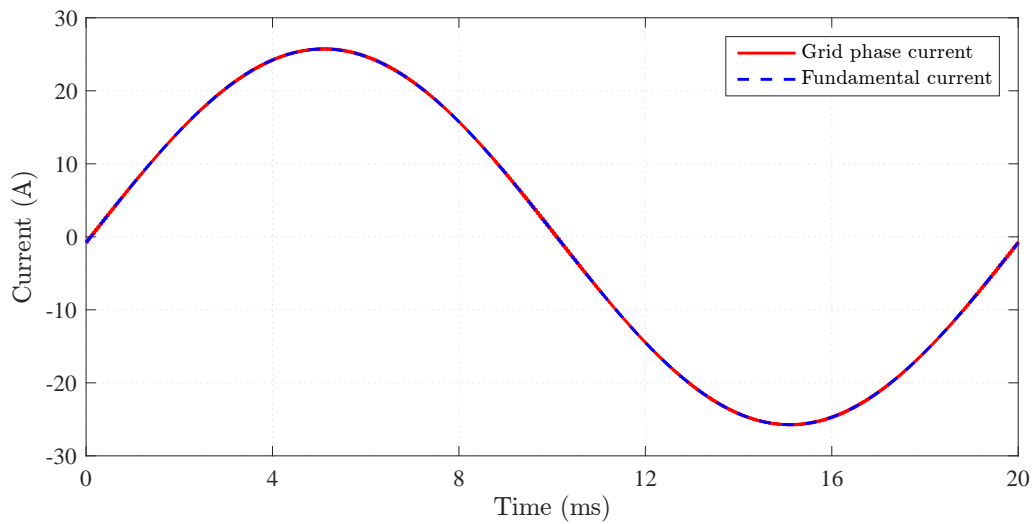


Figure 2.4: Simulated waveform of the grid current.

takes a large percentage of the filter total cost. Considering these cases, the design of the converter-side inductor is emphasized.

The required inductance can be obtained from a single inductor or from multiple smaller inductors. Since the power density of the magnetic component increases with the rated power, a single inductor design is beneficial over multiple inductor design in terms of the weight, volume and power loss. In this thesis, the required converter-side inductance is obtained with a single inductor considering high frequency ripple current and the fundamental component. In the following two sections, fundamentals of magnetic theory and the inductor design procedure are introduced briefly.

# 3 Fundamentals of magnetic theory

The magnetic components have great significance in power electronics and other areas of electrical engineering. These are usually the largest, heaviest and most expensive components in electrical systems. They are defined by their electromagnetic behaviour. In this section, a brief review of the fundamental magnetic relationships and the basic laws are discussed. Magnetic circuits are included together with examples. The analogies between electric and magnetic circuits are presented. Hysteresis and basic properties of the magnetic materials are also discussed.

## 3.1 Electromagnetic laws and relationships

Ampere's law, Faraday's law, Lenz's law, and Gauss's law are the basis of the magnetic circuit analysis. These are the laws that are useful in the design of magnetic components, such as an inductor and transformer.

An inductor with  $N$  turns which is carrying an ac current  $i$  produces the MMF (cf. Fig. 3.1(a)). The MMF is the source in magnetic circuits. The MMF forces the magnetic flux  $\phi$  to flow in the magnetic circuit. The magnetic field intensity  $H$  is defined as the MMF per unit length. According to Ampere's law, the integral of magnetic field intensity  $\mathbf{H}$  around a closed path  $l$  is equal to the total current  $i$  enclosed by that path and passing through the interior of the closed path bounding the surface [17, 27]. Ampere's law can be written as

$$\oint_l \mathbf{H} \cdot d\mathbf{l} = Ni \quad (3.1)$$

The amount of the magnetic flux  $\phi$  passing through a surface  $A_c$  is determined by the surface integral of the magnetic flux density [17]. The magnetic flux density  $B$  is the magnetic flux per unit area. If the magnetic flux density is uniform and perpendicular to surface  $A_c$ , then the amount of magnetic flux passing through the surface is calculated from

$$\phi = BA_c \quad (3.2)$$

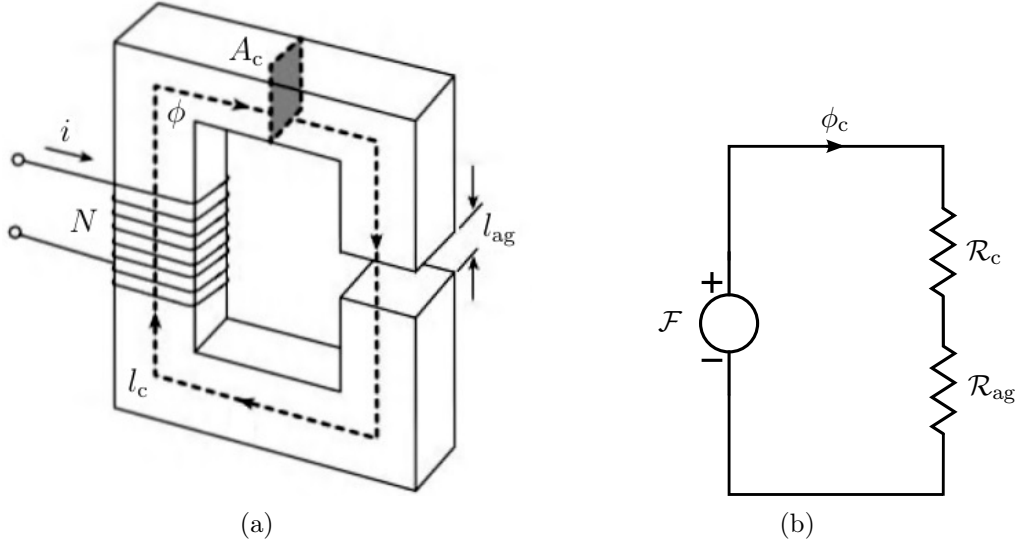


Figure 3.1: Magnetic circuit: (a) an inductor composed of a core with an air gap and winding [17]; (b) equivalent magnetic circuit.

The relationship between the magnetic flux density  $B$  and the magnetic field intensity  $H$  is given by

$$B = \mu H = \mu_0 \mu_r H \quad (3.3)$$

where,  $\mu_0$  is the permeability of free space, and  $\mu_r$  is the relative permeability of the material. The permeability is the measure of the ability of a material to conduct magnetic flux. High permeability materials produce large magnetic flux density with a small current. The peak magnetic flux density  $B_{pk}$ , which consists of all current components, should be lower than the saturation flux density  $B_{sat}$  of the magnetic material,  $B_{pk} \leq B_{sat}$ . [17]

The sum of the flux enclosed by each turn of the wire wound around the core is defined as the magnetic flux linkage [17]. For uniform magnetic flux density, the magnetic flux linkage is the magnetic flux  $\phi$  linking  $N$  turns. For an inductor with core cross sectional area of  $A_c$ , length of  $l$ , the flux linkage can be defined as

$$\psi = N\phi = NA_c B = NA_c \mu H = \frac{\mu A_c N^2 i}{l} \quad (3.4)$$

Faraday's law states that the integral of the electric field intensity  $\mathbf{E}$  around a closed loop  $l$  is equal to the rate of change of the magnetic flux that crosses the surface enclosed by the loop [27, 28]. Faraday's law can be described in differential form as

$$e(t) = -N \frac{d\phi(t)}{dt} \quad (3.5)$$

The negative sign indicates that the current flow in the external circuit will create an opposing magnetic field. When the magnetic flux  $\phi(t)$  links each turn of the coil

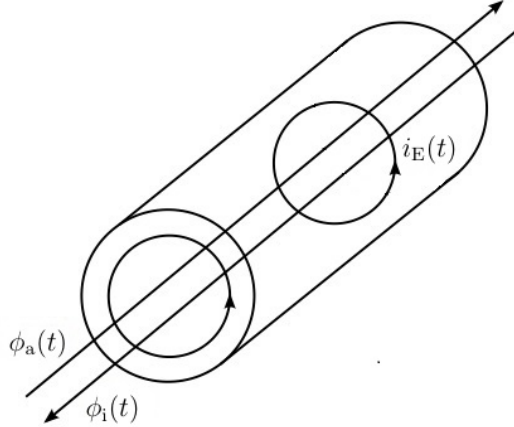


Figure 3.2: Illustration of Lenz’s law.

with  $N$  turns, the induced electromotive force  $e(t)$  in the coil is proportional to the rate of change of the magnetic flux that links the coil [28].

According to Lenz’s law, the voltage  $e(t)$  generated by an applied time varying magnetic flux  $\phi_a(t)$  has such a direction that induces current  $i_E(t)$  in the closed loop, which in turn induces a magnetic flux  $\phi_i(t)$  that tends to oppose the changes in the applied magnetic flux  $\phi_a(t)$  [17]. The induced currents  $i_E(t)$  flowing in the closed loop are called eddy currents, as illustrated in Fig. 3.2. In winding conductors and magnetic cores, the effects of the eddy currents are nonuniform current distribution, increased effective resistance, increased power loss, and reduced internal inductance.

Gauss’s law for magnetic circuit states that the total flux entering the volume is exactly equal to the total flux coming out of the volume for any closed surface [17,27]. According to the law, the net magnetic flux through any closed surface is always zero

$$\oint_S \mathbf{B} \cdot d\mathbf{S} = 0 \quad \Rightarrow \quad \sum_{i=1}^n \phi_i = 0 \quad (3.6)$$

Considering Fig. 3.1(a), the application of Gauss’s law for a closed surface crossing the core and the air-gap and including the total transition surface between them, provides the expression

$$\int \mathbf{B}_c \cdot d\mathbf{S} + \int \mathbf{B}_{ag} \cdot d\mathbf{S} = 0 \quad (3.7)$$

## 3.2 Magnetic circuits

Fig. 3.1(a) shows a coil with  $N$  turns wound on a magnetic core of mean length  $l_c$ , air-gap length  $l_{ag}$ , and core cross-section area of  $A_c$ . The equivalent magnetic circuit is given in Fig. 3.1(b).

### 3.2.1 Reluctance

The reluctance  $\mathcal{R}$  is the resistance of the medium to the flow of the magnetic flux  $\phi$ . The reluctance of the magnetic circuit is directly proportional to the length of the magnetic path and inversely proportional to the cross-section area. This is the analogy with resistance in an electrical circuit. The reluctance of the core  $\mathcal{R}_c$ , and the reluctance of the air-gap  $\mathcal{R}_{ag}$  can be calculated from

$$\mathcal{R}_c = \frac{l_c}{\mu A_c} = \frac{l_c}{\mu_0 \mu_r A_c} \quad (3.8)$$

$$\mathcal{R}_{ag} = \frac{l_{ag}}{\mu A_{ag}} = \frac{l_{ag}}{\mu_0 A_{ag}} \quad (3.9)$$

where  $A_c$  and  $A_{ag}$  are the cross-section area of the core and the air-gap, respectively. Moreover, the reluctance is related to the relative permeability  $\mu_r$  of the material. The relative permeability is a non-linear function of the applied magnetic field intensity in the magnetic materials. However, since the air-gap is introduced in the magnetic circuit, it provides increased equivalent reluctance. The total equivalent reluctance  $\mathcal{R}_{eq}$  of the circuit can be expressed as

$$\mathcal{R}_{eq} = \mathcal{R}_c + \mathcal{R}_{ag} = \frac{l_c}{\mu_0 \mu_r A_c} + \frac{l_{ag}}{\mu_0 A_{ag}} \quad (3.10)$$

### 3.2.2 Magnetic flux continuity

From the application of Ampere's law, the sum of the MMF around a closed magnetic loop is zero

$$\sum \mathcal{F} = 0, \quad \sum \mathcal{F}_{source} = \sum \mathcal{F}_{drop} \quad (3.11)$$

$\mathcal{F}_{drop}$  of the magnetic circuit shown in Fig. 3.1(a) is  $H_c l_c + H_{ag} l_{ag}$ . Considering, (3.2), (3.3), and (3.10),  $\mathcal{F}_{drop}$  of the magnetic circuit becomes

$$\mathcal{F}_{drop} = \phi_c \mathcal{R}_c + \phi_{ag} \mathcal{R}_{ag} \quad (3.12)$$

Here,  $\mathcal{F}_{source}$  of the magnetic circuit is  $Ni$ . The magnetomotive forces of the circuit can be expressed as

$$Ni = H_c l_c + H_{ag} l_{ag} = \phi_c \mathcal{R}_c + \phi_{ag} \mathcal{R}_{ag} \quad (3.13)$$

Further, it is assumed that the magnetic flux  $\phi_c$  of the core is equal to the magnetic flux  $\phi_{ag}$  of the air-gap. Substituting,  $\phi_c = \phi_{ag} = \phi$ , (3.13) can be written as

$$\mathcal{F} = Ni = \phi_c \mathcal{R}_c + \phi_{ag} \mathcal{R}_{ag} = \phi (\mathcal{R}_c + \mathcal{R}_{ag}) \quad (3.14)$$

Equations (3.7) and (3.14) are valid only for small air gaps (fringing flux neglected). At larger air gaps, the flux tends to the outside.

### 3.3 Inductance

An inductor is a two-terminal passive device that is able to store magnetic field and energy in this magnetic field. The inductance depends on (i) winding geometry (ii) core and bobbin geometry (iii) permeability of the core material and (iv) frequency [17]. The following methods can be used to determine the inductance.

#### Magnetic flux linkage method

The inductance for linear and non-linear inductors is defined as the ratio of the magnetic flux linkage  $\psi$  to the ac current  $i$  producing the flux linkage

$$L = \frac{\psi}{i} \quad (3.15)$$

The total inductance of an inductor has two components: an external inductance  $L_{\text{ext}}$  and an internal inductance  $L_{\text{int}}$

$$L = L_{\text{ext}} + L_{\text{int}} = \frac{\psi_{\text{ext}}}{i} + \frac{\psi_{\text{int}}}{i} \quad (3.16)$$

External magnetic energy stored in the magnetic field outside the conductor produces the external inductance. External inductance is independent of frequency. The internal inductance is due to the internal magnetic energy stored in the magnetic field inside the conductor. Internal inductance depends on the frequency. The magnetic field intensity  $H$  inside the conductor is a function of frequency due to skin effect. The internal inductance usually decreases with frequency [17].

#### Reluctance method

The inductance of an inductor can be determined using the total number of turns  $N$  and the reluctance  $\mathcal{R}$  of the magnetic circuit. The inductance of an inductor is inversely proportional to the reluctance. Using (3.4) and (3.15), the inductance can be calculated as

$$L = \frac{N^2 \mu_r \mu_0 A_c}{l} = \frac{N^2}{\mathcal{R}} \quad (3.17)$$

#### Magnetic energy method

The current flowing through the inductor generates the magnetic field where the energy is actually stored. The energy stored by an inductor is equal to the amount of work required to establish the current through the inductor. The stored energy  $W_L$  can be defined as

$$W_L = \frac{1}{2} L I_{\text{pk}}^2 \quad (3.18)$$

This relationship is only valid for linear regions of the magnetic flux linkage and current relationship.

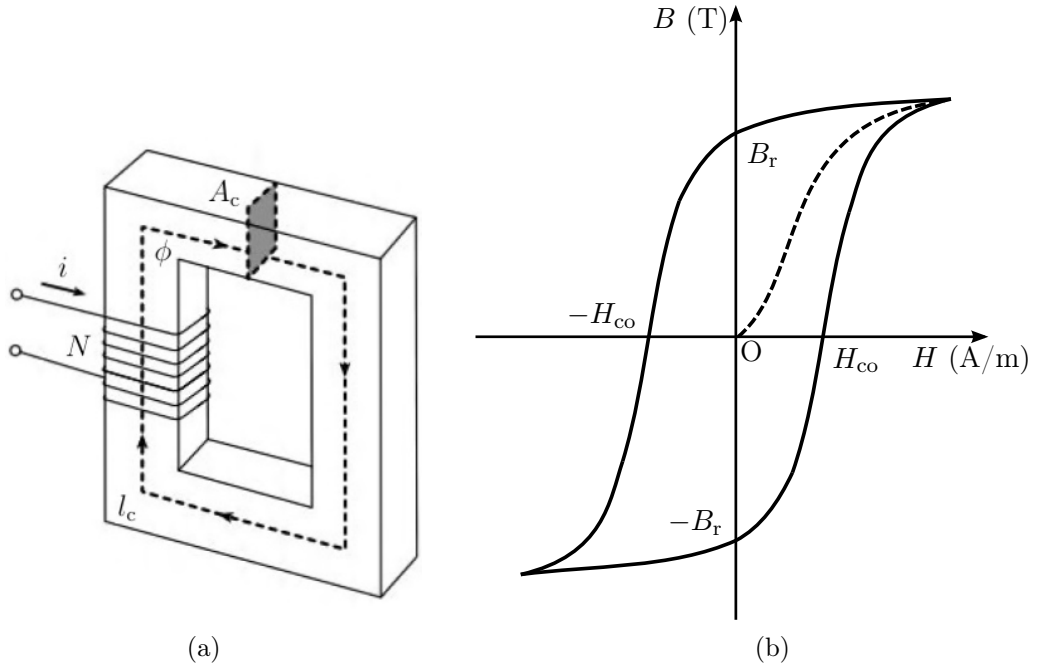


Figure 3.3: Illustration of magnetic hysteresis: (a) a magnetic core with a coil carrying a current  $i$  [17]; (b) typical hysteresis loop and magnetization curve of the magnetic core.

### 3.4 Magnetic hysteresis

A magnetic core with a coil carrying a current  $i$  shown in Fig. 3.3(a) can be considered for describing the hysteresis loop. The core material is taken through a complete cycle of magnetization and demagnetization. The current  $i$  in the coil, the magnetic field intensity  $H$ , and the magnetic flux density  $B$  are zero at the beginning. Increasing the current slowly in the coil results in the magnetic field intensity in the core according to Ampere's law. As the magnetic field intensity  $H$  is increased, the flux density increases along the dashed line. Increase in  $H$  to larger values results in non-significant increase in  $B$ , the material reaches saturation. At the saturation point, all the atomic magnets are aligned along the direction of the applied external field. When  $H$  is decreased, the flux does not return along the same curve. When  $H$  reaches to zero, the core is still magnetized. The flux density at this point is called the remanence flux density  $B_r$ . To reduce the flux density  $B$  to zero, a reversed magnetic field is needed to be applied. The value of  $H$  at which the flux density reaches to zero is called coercive field of the material  $H_{co}$ . A further increase of  $H$  in the opposite direction results in a process of magnetization as the one described above. The magnetic flux density  $B$  reaches saturation point. If the current of the excitation coil is repeatedly cycling for generating two opposite maximum values of  $H$ , the hysteresis loop is traced out as shown in Fig. 3.3(b). The loop shows that the relationship between the magnetic flux density  $B$  and the magnetic field intensity  $H$  is non-linear and multivalued [27, 29]. Throughout the cycle of magnetization and

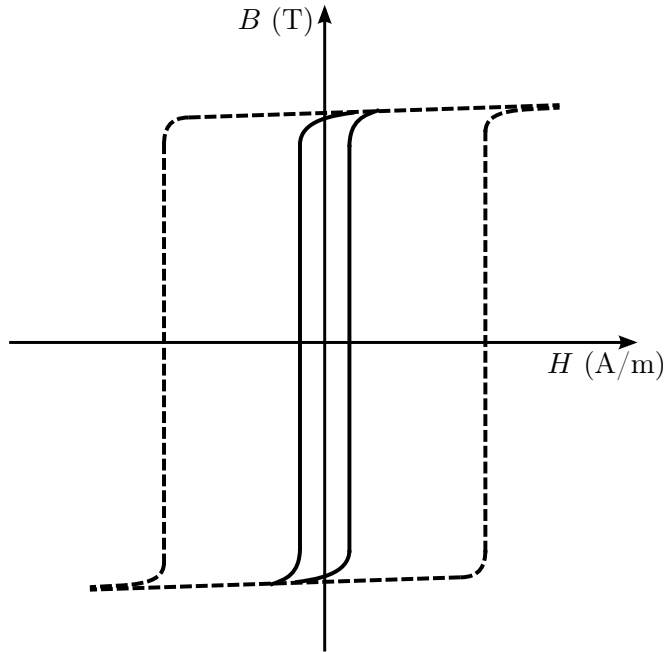


Figure 3.4: Typical hysteresis loops:(a) a soft magnetic material, narrow loop (solid line); (b) a hard magnetic material, larger loop (dashed line).

demagnetization, the magnetic flux density lags behind the magnetic field intensity. This lagging phenomenon in the magnetic core material is called hysteresis.

The energy flowing from the source is greater than the energy returned. Therefore, the enclosed area of the loop is a measure of energy loss in the core material during the cycle of variation. This energy loss generates heat in the core. The loss of power due to hysteresis effect is called hysteresis loss. The area of hysteresis loop is proportional to the hysteresis loss. The area of hysteresis loop is dependent on the excitation frequency, increasing the frequency larger the area of hysteresis loop. The shape of the hysteresis loop is also material dependent. Soft magnetic materials, such as iron-silicon alloys, amorphous and nanocrystalline alloys, are easy to magnetize and demagnetize. Thus, soft magnetic materials provide low coercive force and narrow hysteresis loop. Hard magnetic materials, such as alnicos, iron-neodymium, iron-chromium-cobalt, retain their magnetism even after the removal of the applied magnetic field. The hard magnetic materials produce flux even without any external field, and provide high coercive force [27]. Fig. 3.4 shows the typical hysteresis loop of soft and hard magnetic materials.

### 3.5 Air-gap in magnetic core

In the magnetic circuit without any air-gap, the flux is limited only by the core material. A small amount of current with sufficient turns can easily drive the magnetic core material into saturation. However, if a gap is introduced into the core, a larger

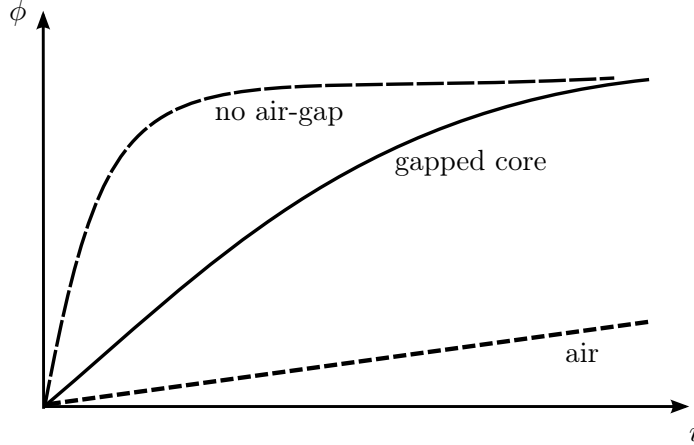


Figure 3.5: Magnetization curve for air, no air-gap and gapped core.

current will be required to achieve saturation of the magnetic material due to the increased reluctance introduced by the air-gap. The equivalent reluctance of the gapped core can be calculated using (3.10). If the cross-sectional area of the core  $A_c$  is equal to the cross-sectional area of the air-gap  $A_{ag}$ , then (3.10) can be written as

$$\mathcal{R}_{eq} = \frac{l_c}{\mu_0 A_c} \left( \frac{1}{\mu_r} + \frac{1}{\frac{l_c}{l_{ag}}} \right) = \frac{l_c}{\mu_{eff} \mu_0 A_c} \quad (3.19)$$

where,  $\mu_{eff}$  is the relative permeability of the magnetic circuit with a gapped-core. The gap reduces the effective permeability of a magnetic circuit. Equation (3.19) means that, the reluctance of the gapped core is equal to the reluctance of a core with length  $l_c$  and with relative permeability  $\mu_{eff}$ , where

$$\mu_{eff} = \frac{1}{\frac{1}{\mu_r} + \frac{1}{l_c/l_{ag}}} \quad (3.20)$$

Equation (3.19) shows that the overall reluctance of the gapped core  $\mathcal{R}_{eq}$ , the inductance  $L$ , the magnetic flux  $\phi$ , and the magnetic flux density  $B$  can be controlled by the air-gap length  $l_{ag}$ . The winding must have more number of turns to get the required inductance, as the increasing of the air-gap length reduces the inductance. The magnetization curve of a magnetic circuit is affected by the presence of an air-gap. Since the permeability of the non-magnetic material is low, larger value of current is required with the air-gap to obtain the same value of  $\phi$  in comparison with the magnetic circuit without air-gap. Fig. 3.5 shows the air-gap effect on the magnetization curve. The value of the slope is proportional to the effective permeability of the magnetic circuit. The effective permeability is reduced for the gapped core, larger the air-gap lower the slope. On contrast, the slope becomes as steep as possible if no air-gap is present. Higher currents can be tolerated before the onset of saturation at the expense of lower value of inductance in the gapped core. It is observed from Fig. 3.5 that the air-gap in the magnetic circuit increases

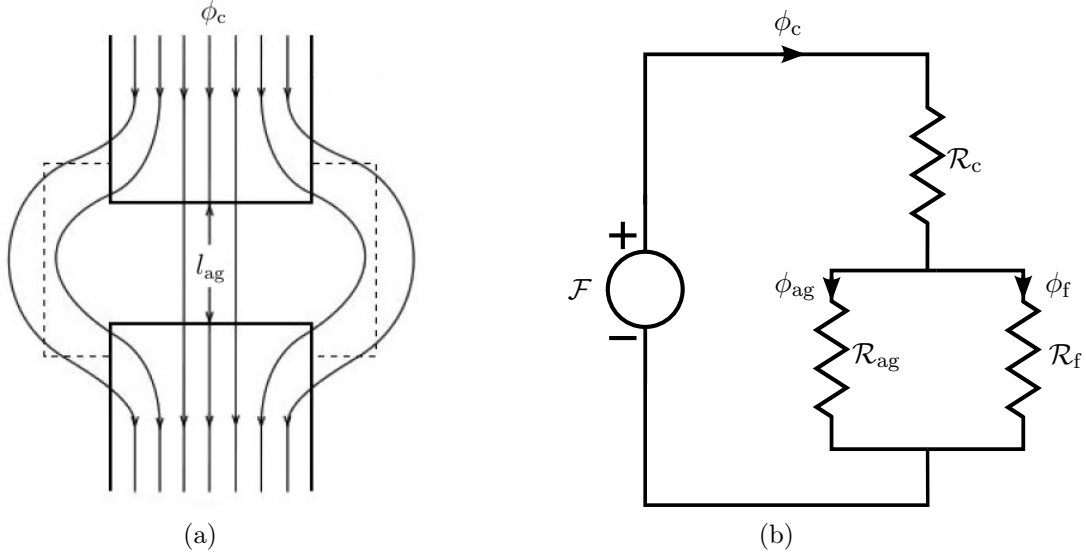


Figure 3.6: Illustration of fringing flux: (a) fringing magnetic flux in an air-gap [17]; (b) magnetic equivalent circuit of an inductor with an air-gap and a fringing magnetic flux.

the linear part of the magnetization curve, meaning that inductance remains constant with changing in current. Furthermore, the losses in the magnetic core are less frequency-dependent due to the presence of air-gap.

However, the air-gap generates fringing flux which increases proximity and eddy current losses in conductors located in the vicinity of the air-gap. The air-gap can be distributed into many smaller gaps in order to reduce the flux fringing effect and the losses associated with it. Small particles are bound together in such a way that the magnetic materials contain a certain percentage of non-magnetic volume in them. The air-gap is uniformly distributed throughout the whole material. Thus, the resultant effective permeability is much lower. Such cores are usually more expensive than others with a single air-gap.

### 3.6 Fringing flux

The expression for reluctance of a gapped core in (3.19) assumes that there are no fringing effects around the air-gap. In practice, the flux lines do not cross the air-gap in straight lines. The fluxes bulge outward as the magnetic lines repel each other when passing through a non-magnetic material as shown in Fig. 3.6(a). The cross sectional area of the magnetic field is increased and the flux density decreased. This effect is called fringing flux effect. According to [17], 10% is a typical value by which the cross-sectional area has to be increased. However, the cross-sectional area can be increased as a function of the air-gap length  $l_{ag}$  to get the proper value of air-gap and cross-section area. The effective cross section area of the gap with fringing flux can be obtained by adding the air-gap length  $l_{ag}$  to each of the linear dimensions of

the core in the air gap [28].

The fringing reluctance  $\mathcal{R}_f$  is shunting the air-gap reluctance  $\mathcal{R}_{ag}$ , reducing the equivalent reluctance  $\mathcal{R}_{eq}$  and the overall inductance  $L$  is increased by a factor of  $F_f$ .  $F_f$  is called the fringing flux factor. The number of turns  $N$  can be decreased or the air-gap length  $l_{ag}$  can be increased for obtaining the desired inductance [17]. Fig. 3.6(b) represents the magnetic equivalent circuit of an inductor with an air-gap including the fringing magnetic flux  $\phi_f$ . Due to the continuity of the magnetic flux (3.7), the magnetic flux in the core  $\phi_c$  is equal to the sum of the magnetic flux in the air-gap  $\phi_{ag}$  and the fringing flux  $\phi_f$

$$\phi_c = \phi_{ag} + \phi_f \quad (3.21)$$

### 3.7 Losses in magnetic components

In an inductor, losses can be categorized into winding losses and core losses. The winding losses can be divided into the dc loss and the ac loss. Winding dc loss can be expressed from the dc resistance of the coil. However, winding ac loss is needed to calculate the actual winding loss at high frequency considering skin and proximity effects. The actual winding ac resistance can be obtained from the frequency-dependent inductor model presented in [14]. Based on the analytical model for an inductor as a function of frequency given in [15–17], the winding model has less effect to the total resistance and inductance. The winding resistance and the leakage inductance are negligible as compared to the core equivalent resistance and main inductance, respectively.

Core loss can be divided into hysteresis loss and eddy current loss. Energy loss  $W_{cycle}$  over one cycle of the hysteresis loop in the core can be expressed as (cf. Fig. 3.3(b))

$$W_{cycle} = V_c \oint H dB = V_c w_h \quad (3.22)$$

where  $V_c$  is the volume of the magnetic core, and  $w_h = \oint H dB$  is the energy loss density in the core [30]. The power loss  $P_h$  in the core due to hysteresis effect can be expressed as  $P_h = V_c w_h f$ , where  $f$  is the frequency of variation of the current. Under the assumption provided by Charles Steinmetz, the hysteresis loss can be defined as

$$P_h = K_h B_{pk}^m f \quad (3.23)$$

where  $K_h$  is a constant,  $B_{pk}$  is the peak flux density, and  $m$  varies in the range 1.5 to 2.5. The value of constant  $K_h$  depends on the ferromagnetic material and the volume of the core.

Rapid changes of the flux density in the core generates another power loss. Fig. 3.7(a) shows the cross section of the core through which the flux density  $B$  is rapidly changing. The voltage is induced in the path of the cross-section due to the time-varying magnetic flux enclosed by the path. Consequently, the large circulating eddy

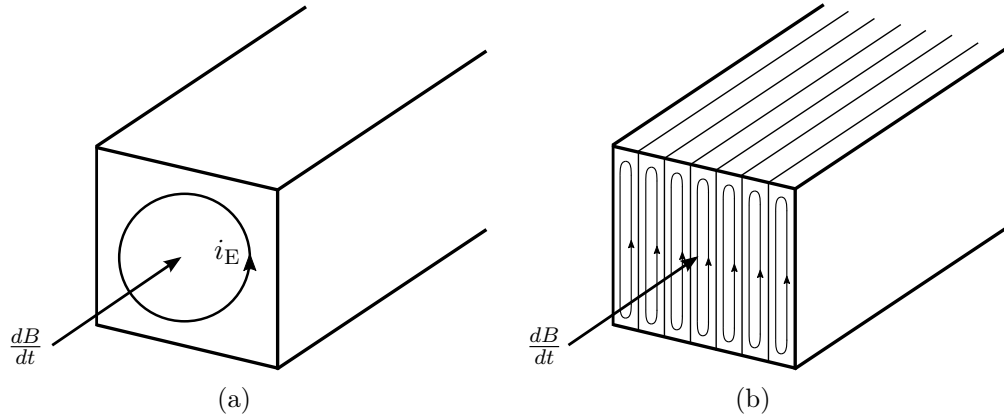


Figure 3.7: Illustration of eddy current in a magnetic core: (a) solid core; (b) laminated core.

current  $i_E$  flows around the path. The eddy current  $i_E$  produces power loss due to the conductivity of the core material and appears as heat in the core. The eddy current loss can be reduced using high-resistivity and laminated core material (cf. Fig. 3.7(b)). Consequently, the circulating current in each lamination is less than the large circulating eddy current. The eddy current loss  $P_e$  in the magnetic core due to the time-varying magnetic flux can be expressed as

$$P_e = K_e B_{pk}^2 f^2 \quad (3.24)$$

where  $K_e$  is a constant whose value depends on magnetic material and lamination thickness [30]. Lamination thickness varies from 0.01 to 0.5 mm in devices used in power electronic circuit operating at high frequencies. The hysteresis loss and eddy current loss are lumped together to get the total core loss as  $P_c = P_h + P_e$ .

## 4 Design of an inductor

The subject of this section is to design a compact converter-side inductor of an LCL filter connected to a SiC grid converter. The area product method is used. A step-by-step design procedure for the inductor is given. The core material is selected based on the peak flux density. The core material selection is followed by the core shape, size, and the winding design.

### 4.1 Area product method

The area product is defined by the product between the window area and the cross-sectional area of the core (cf. Fig. 4.1)

$$A_p = W_a A_c = \frac{2W_L}{K_u J_m B_{pk}} \quad (4.1)$$

where  $W_a$  is the window area of the core,  $A_c$  is the cross-sectional area of the core,  $K_u$  is the window utilization factor,  $J_m$  is the rms value of current density, and  $B_{pk}$  is the peak flux density of the core material [17]. The inductor energy  $W_L$  is directly proportional to the inductor area product  $A_p$ . Further, the inductor energy  $W_L$  depends on the value of the inductance  $L$  and the maximum current  $I_{pk}$  flowing through the inductor. Thus, a compact size is achieved by minimizing the value of the inductor energy. The area product value gives a rough initial estimate of the core size satisfying both the electromagnetic conditions and the restriction of the core window area. The left-hand side of (4.1) contains the core dimensions and the right-hand side includes the inductor electrical and magnetic properties.

### 4.2 Inductor design algorithm

Fig. 4.2 shows the flowchart of the inductor design algorithm. The linear part of the magnetization curve is assumed in the algorithm. Electrical and magnetic parameters are the inputs into the algorithm. The inductor size is strongly influenced

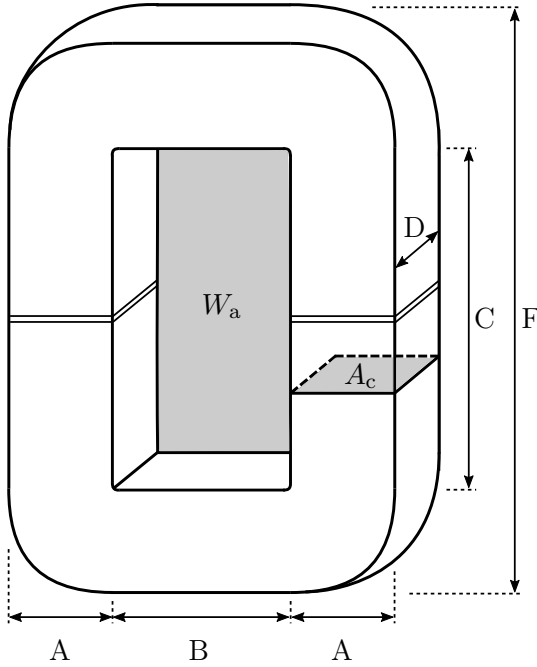


Figure 4.1: Illustration of the area product using a pair of c-cut core.

by the magnetic material properties, operating current, and cooling condition. The core size is selected by applying an iterative design procedure. The algorithm calculates the following factors: rounded up number of turns, winding layers, air-gap length, and fringing flux factor. The winding skin and proximity effects, the losses, and the temperature rise are also considered. The algorithm is performed in the following way.

First, the electric specifications are declared including the switching frequency  $f_{sw}$ , converter rms current  $I_{rms}$ , peak value of converter current  $I_{pk}$ , peak value of fundamental current  $I_{1,pk}$ , peak-to-peak ripple current  $I_{sw,pk-pk}$ , and inductance  $L$  (cf. Fig. 2.3). Secondly, the magnetic material properties are defined by the relative magnetic permeability  $\mu_r$ , saturation flux density  $B_{sat}$ , mass of the core  $m_c$ , core fill factor  $k_c$ , core loss density  $p_v$ , and the Steinmetz equation parameters  $k$ ,  $\alpha$ , and  $\beta$ . Thirdly, the winding geometry are defined by conductor rms current density  $J_m$ , conductor diameter  $d$ , nominal outer diameter  $d_o$ , the area of bare conductor  $A_w$ , and the conductor total cross-section area  $A_{w,tot}$ .

After that, the area product is calculated from (4.1) using the electric specifications, magnetic materials, and winding properties. The core is selected from the several core shapes based on the calculated area product value. The core dimensions shown in Fig. 4.1 declare the core width  $A$ , window width  $B$ , window length  $C$ , and core height  $D$ . The initial core dimension variables must be set in the algorithm for the area product calculation. Then, the number of turns  $N$  and the air-gap length  $l_{ag}$  are calculated by applying an iterative process to obtain the required inductance  $L$  and the peak flux density. The magnetic circuit model is used to calculate the air-gap length  $l_{ag}$  considering the fringing flux factor  $F_f$ .

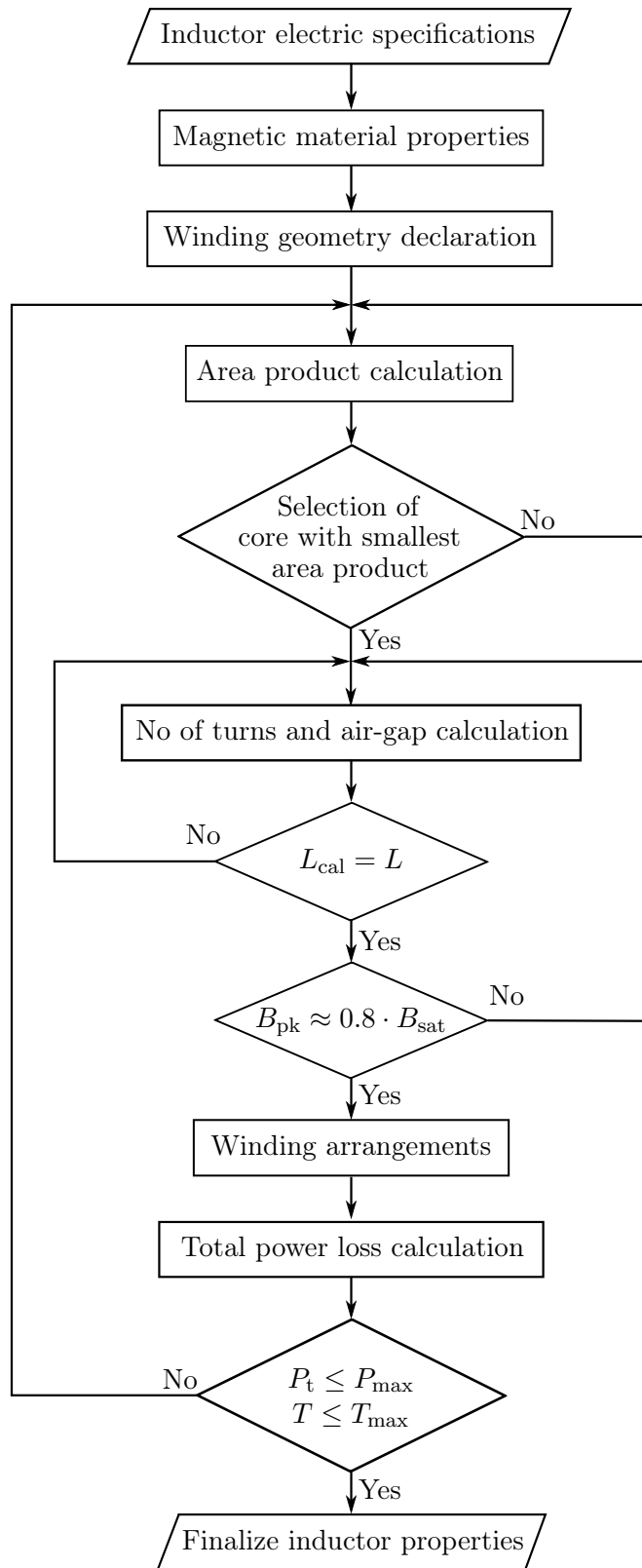


Figure 4.2: Design algorithm of the inductor.

The winding geometry and arrangements allow the calculation of the number of turns per layer  $N_{tl}$ , number of layers  $N_l$ , and the conductor length  $l_w$ . The conductor material sets the material electrical resistivity  $\rho_w$ , the conductor relative magnetic permeability  $\mu_{rw}$ , and the dc resistance per length. The dc resistance  $R_{w(dc)}$  and the corresponding winding loss  $P_{w(dc)}$  are calculated. Then, the total winding loss  $P_w$  is calculated using the winding ac resistance  $R_{w(ac)}$  expressed by Dowell's Equation [14]. The core loss  $P_c$  is calculated using the Steinmetz equation. Next, the inductor total power loss  $P_t$  is calculated. Inductor thermal modeling is considered to calculate the temperature rise  $\Delta T$ . The rise in temperature caused by the losses should not exceed the maximum rise in temperature. Finally, the inductor properties are gathered. The inductor is characterized by its outer dimensions as: width  $w_i$ , length  $l_i$ , height  $h_i$ , total mass  $m_i$ , and the inductor volume  $V_i$ .

## 4.3 Magnetic material

The optimum choice of the magnetic material for an inductor design is not straightforward. The material is limited by the saturation flux density and core loss density. In this thesis, the material is selected based on the highest peak flux density. The material should have high peak flux density within the limits defined by the saturation flux density and core loss density. The system cooling condition, size, and cost requirements also determine the preferred option.

### 4.3.1 Magnetic material properties

The typical specifications for the magnetic materials of interest are shown in Table 4.1. The 10JNHF600 silicon steel has the highest saturation flux density and thermal conductivity. The continuous operating temperature of 150 °C is similar to the 2605SA1 amorphous material. However, 10JNHF600 has a greater thickness of lamination than that of 2605SA1 and the nanocrystalline materials. This results in the 10JNHF600 core material having higher eddy-current core loss. The Vitrop-erm500F nanocrystalline material and the 3C93 ferrite material are low core-loss materials. These materials have lower saturation flux densities and lower operating temperatures as well. The nanocrystalline material has the best overall characteristics, but it is significantly more expensive than the other materials. The significant advantage of the 3C93 ferrite material is its high resistivity [19]. Unlike the other materials, due to its bulk composition and high resistivity, 3C93 does not suffer from additional eddy-current core losses due to fringing of the air gap. The saturation flux density of the Xflux and High-flux powder core is similar to 2605SA1 amorphous. The continuous operating temperature of 200 °C is the highest among the materials, though the thermal conductivity is less in comparison with others. Further, Xflux and High-flux powder core materials have higher core losses.

The core maximum operating temperature is limited theoretically by the Curie temperature. However, practically the temperature is limited by the lamination and

Table 4.1: Typical magnetic properties of different core materials [19].

| Material type   | Material      | Saturation flux density (T) | Continuous operating temperature (°C) | Thermal conductivity (W/mK) | Core loss @ 0.1 T, 20 kHz (mW/cm³) |
|-----------------|---------------|-----------------------------|---------------------------------------|-----------------------------|------------------------------------|
| Amorphous       | 2605SA1       | 1.56                        | 150*                                  | 10**                        | 70                                 |
| Silicon steel   | 10JNHF600     | 1.88                        | 150*                                  | 18.6**                      | 150                                |
| Nanocrystalline | Vitroperm500F | 1.2                         | 120*                                  | 10**                        | 5                                  |
| Ferrite         | 3C93          | 0.52                        | 140                                   | 3.5-5                       | 5                                  |
| Powder core     | Xflux         | 1.6                         | 200                                   | 8                           | 200                                |
| Powder core     | High-flux     | 1.5                         | 200                                   | 8                           | 100                                |

\*limited by the lamination epoxy, \*\*along laminations

coating thermal capability limits. The 2605SA1, 10JNHF600 and Vitroperm500F materials are limited by the lamination epoxy thermal capability. Elevated temperature may trigger thermal ageing due to material recrystallization in case of Vitroperm500F. The maximum temperature of powder cores is limited by the coating thermal capability. The ferrite material is generally designed to operate at the unique material temperature at which the specific core loss is minimum for a given flux density in order to avoid the core thermal runaway. These temperatures are typically in the range of 80–150 °C for ferrites [19, 31].

#### 4.3.2 Magnetic material selection

The first step in the designing of an inductor is the core material selection. The particular core material defines the key magnetic properties such as the saturation flux density and core-loss density. The converter-side inductor has higher ripple current than the grid-side inductor. The high current ripple causes higher core losses. To avoid overheating, the core losses should be kept low enough. This sets higher demands on the core material, which has to be properly selected. The core material can be selected based on the peak flux density. In order to minimize the area product (4.1), the peak flux density  $B_{pk}$  should be as high as possible.

The peak flux density  $B_{pk}$  is limited to upper boundary set by the saturation flux density  $B_{sat}$  of the material. Typically, the boundary is set to 80-90% of the saturation flux density  $B_{sat}$  [32, 33]. This boundary is introduced to avoid operation close to saturation point. The material can be selected with the high saturation flux density and low power losses in the core to keep the temperature rises beyond the maximum temperature margin  $T_{max}$ . The core-loss density gives a rough estimate for evaluating the temperature rise. A thermal model can be included in the design to ensure that the operating temperature is kept within safe values. If the core temperature rises beyond the temperature margin with the selected peak flux density and the core-loss density, the design is discarded and a new design process is started with a new set of free parameters.

A comparison chart showing the saturation flux density versus core loss at a given frequency and flux density is given in Fig. 4.3. The 3C93 core material is limited

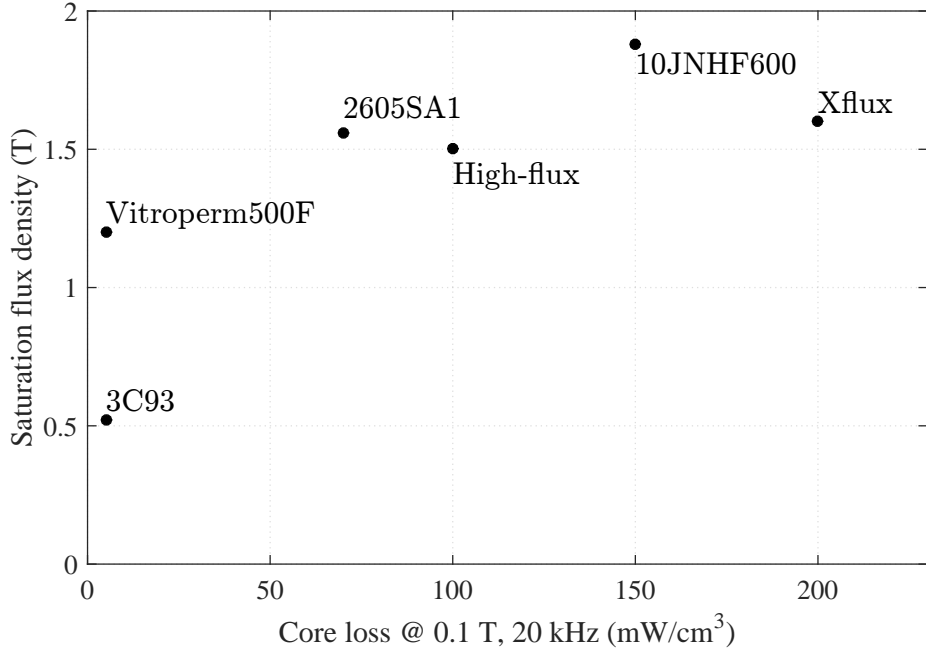


Figure 4.3: Comparison of different core materials.

by the saturation flux density. The low saturation flux density and the low allowed temperature rise result in the largest inductor with the 3C93 material for the analyzed frequency. The Vitroperm500F core material has also low saturation flux density and low core-loss density in comparison with other materials. The 2605SA1, 10JNHF600, Xflux and High-flux materials are limited by their core-loss density. The 2605SA1, Xflux and High-flux materials have almost similar saturation flux density in the range of 1.5-1.6 T. However, the Xflux and the High-flux materials have lower thermal conductivity and higher core-loss density in comparison with the 2605SA1 material.

The 2605SA1 and the 10JNHF600 materials are competitive and lead to the smallest size inductor for the analyzed frequency. The 10JNHF600 material is a high core loss material resulting in a larger core for a given temperature rise. However, it is worth noting that the 10JNHF600 has the highest saturation flux density. Under natural convection conditions, the optional material for smallest size inductor is 2605SA1. Further, size reduction can be achieved by using improved cooling methods such as air-forced convection and conductive cooling. Under air-forced convection, both the 2605SA1 and the 10JNHF600 materials can be used. If a conductive cooling path is provided for the core, the performance of the 10JNHF600 material will likely improve due to the higher thermal conductivity of 18.6 W/mK [34].

### 4.3.3 Peak flux density calculation

The VSC output contains significant harmonics around the switching frequency. It is assumed that all the high frequency ripple current is packed on the switching frequency. Thus, the flux waveform contains a fundamental sinusoidal waveform and superimposed high frequency ripples. The fundamental waveform results the larger loop, while the the high frequency ripples result smaller loops in the traversed B-H curve. The total peak flux density can be expressed as

$$B_{\text{pk}} = B_{1,\text{pk}} + B_{\text{sw,pk}} \quad (4.2)$$

where  $B_{1,\text{pk}}$  and  $B_{\text{sw,pk}}$  are the peak flux density caused by the fundamental component and the ripple current, respectively. The inductor is designed in such a way that the peak flux density  $B_{\text{pk}}$  corresponds the peak current  $I_{\text{pk}} = I_{1,\text{pk}} + \Delta I_{\text{sw,pk-pk}}/2$  of the converter, where  $I_{1,\text{pk}}$  is the peak value of the fundamental current and  $\Delta I_{\text{sw,pk-pk}}$  is the peak to peak value of the ripple current. The peak flux density  $B_{\text{pk}}$  caused by peak current  $I_{\text{pk}}$  can be calculated using the following formula [17, 34]

$$B_{\text{pk}} = \frac{LI_{\text{pk}}}{NA_{c,\text{eff}}} \quad (4.3)$$

where  $A_{c,\text{eff}} = k_c A_c$  is the effective cross-sectional area of the core. In addition, it is assumed that the flux density is directly proportional to the current below the peak value. The peak flux density caused by the fundamental component  $B_{1,\text{pk}}$  and the peak flux density caused by the ripple current  $B_{\text{sw,pk}}$  can be obtained using the following formulas

$$B_{1,\text{pk}} = \frac{I_{1,\text{pk}}}{I_{1,\text{pk}} + \Delta I_{\text{sw,pk-pk}}/2} B_{\text{pk}}, \quad B_{\text{sw,pk}} = \frac{\Delta I_{\text{sw,pk-pk}}/2}{I_{1,\text{pk}} + \Delta I_{\text{sw,pk-pk}}/2} B_{\text{pk}} \quad (4.4)$$

## 4.4 Winding wire selection

The second step of the inductor design is the selection of winding wire. The winding wire selection involves rms current density, the conductor shape, conductor size, and insulation.

### 4.4.1 Maximum current density

The rms current density  $J_m$  should be as high as possible in order to minimize the area product defined by (4.1). The rms current density  $J_m$  can be selected by considering the cooling conditions of the system. The typical values of the maximum rms current density under natural cooling condition are in the range of 6-10 A/mm<sup>2</sup> when the wire is short ( $l_w < 1$  m) with a small number of turns. The typical value of the maximum rms current density is 5 A/mm<sup>2</sup> for long wire ( $l_w > 1$  m) with a large number of turns [17]. For air-forced cooling condition, the maximum rms current

density is assumed to be higher than the natural cooling condition. In this thesis, the rms current density is assumed to be  $3 \text{ A/mm}^2$  and  $6 \text{ A/mm}^2$  for natural and air-forced cooling condition, respectively.<sup>1</sup>

#### 4.4.2 Conductor selection

Typically, the high eddy current losses associated with the high-ripple current leads to either a foil or litz winding configuration in order to reduce the skin and proximity effects. Moreover, the foil or litz winding configuration provides thermal and mechanical advantages. The spiral winding structure or the edge-wound winding structure can be used for low-ripple current [34]. For simplicity, a single round wire is selected for the design. The choice of conductor is either copper or aluminium for single wire winding. The inductor design with copper wire reduces about 20% the power loss in comparison with the aluminium wire while keeping the same weight [4]. Thus, the enamel-coated round copper wire is considered for the design. The diameter of the wire must be large enough to carry the rms current density  $J_m$ . The area of the bare conductor  $A_w$  is obtained using assumed current density:

$$A_w = \frac{I_{\text{rms}}}{J_m} \quad (4.5)$$

The typical bare conductor can be selected from the IEC 60317-0-1 standard [35] according to the obtained value. The corresponding nominal bare wire diameter  $d$ , nominal outer diameter  $d_o$ , and other characteristics can also be obtained from the IEC 60317-0-1 standard. The value of rms current density  $J_m$  can be recalculated using (4.5) in order to obtain actual rms current density to be used for calculating area product (4.1).

### 4.5 Core geometry selection

Selection of the core is the next step for the designing an inductor. The inductor of each phase are assumed to have the same geometry. A core window must provide sufficient space for winding in the bobbin of the inductor. The core also must provide enough air space between the insulated wire turns. The area product of the core can be obtained using (4.1) and the required core is selected based on the value of area product from the standard core specifications. The core dimension variables such as core width  $A$ , window width  $B$ , window length  $C$ , and core height  $D$  are given by the manufacturers. The core dimension variables allow for further calculations of

---

<sup>1</sup>The existing experimental setup of a 12.5-kVA grid-connected converter in Aalto University School of Electrical Engineering has an LCL filter with  $L_{\text{fc}} = 575 \mu\text{H}$ ,  $C_f = 8.10 \mu\text{F}$ , and  $L_{\text{fg}} = 250 \mu\text{H}$  [23]. The inductors are designed under natural cooling condition with the rms current density  $J_m = 3 \text{ A/mm}^2$ . In addition, the laboratory has an another set of LCL filter with  $L_{\text{fc}} = 2.94 \text{ mH}$ ,  $C_f = 10 \mu\text{F}$ , and  $L_{\text{fg}} = 1.96 \text{ mH}$  [24]. In this case, the inductors are designed under air-forced cooling condition with  $J_m = 6 \text{ A/mm}^2$ .

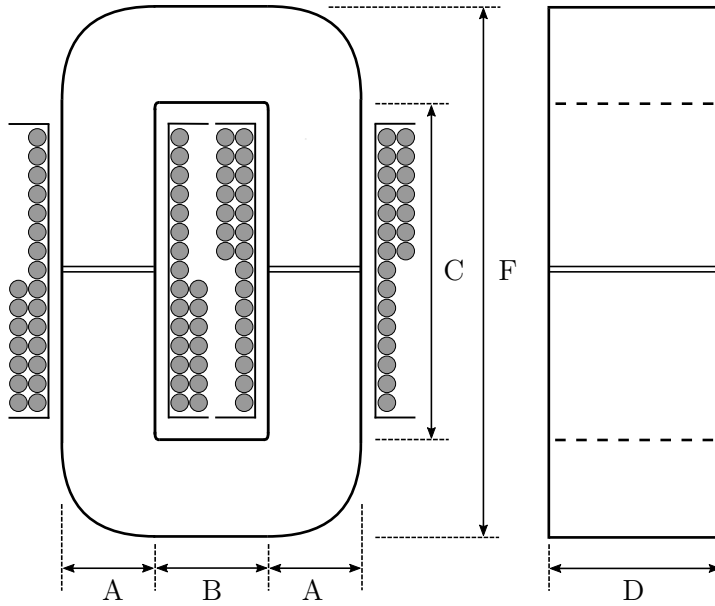


Figure 4.4: Cross-section view of c-cut core with winding configuration.

the core mean magnetic path length  $l_c$ , the core cross-section area  $A_c$ , the effective cross-section area  $A_{c,\text{eff}}$ , window area  $W_a$ , the area product  $A_p$ , and the volume of core  $V_c$ . The inductor consists of two c-cut cores arranged as in Fig. 4.4.

## 4.6 Number of turns calculation

The total number of turns must fit through the core window area. The total area of the copper in the window with  $N$  turns can be expressed as  $NA_w$  and the area available for the conductors can be expressed as  $K_u W_a$ , where  $K_u$  is the window utilization factor. The value of the window utilization factor  $K_u$  depends on the air and wire insulation factor, the bobbin factor, and the edge factor. The typical value of the window utilization factor is 0.4 for inductors [17, 29]. The maximum number of turns  $N_{\max}$  which can be fitted inside the window area  $W_a$  can be obtained using the following formula

$$N_{\max} A_w \leq K_u W_a \quad (4.6)$$

To avoid core saturation and to satisfy the required peak flux density  $B_{\text{pk}}$ , and to obtain the required inductance  $L$ , the number of turns is calculated using (4.3). After finalizing the total number of turns  $N$ , the maximum number of turns per layer  $N_{\text{tl}}$  and the number of winding layers  $N_l$  can be obtained using bobbin specifications. From the height of the bobbin  $H_b$  and the nominal outer diameter  $d_o$ , the maximum number of turns per layer can be calculated using with the following formula

$$N_{\text{tl}} = \frac{H_b}{d_o} \quad (4.7)$$

The number of the winding layers  $N_l$  can be expressed as

$$N_l = \frac{N}{N_{tl}} \quad (4.8)$$

Core and bobbin dimensions give a rough estimate for the length of the winding wire. The wire length per single turn of the first layer  $l_{T,1}$  and the second layer  $l_{T,2}$  of each leg can be expressed as  $l_{T,1} = 2A + 2D + 4B_t$  and  $l_{T,2} = 2A + 2D + 4B_t + 4d_o$ , respectively, where  $B_t$  is the bobbin thickness,  $A$  is the core width and  $D$  is the core height. The length of the winding wire  $l_w$  can be obtained using following equation

$$l_w = 2(N_{tl,1}l_{T,1} + N_{tl,2}l_{T,2}) \quad (4.9)$$

where  $N_{tl,1}$  and  $N_{tl,2}$  are the number of turns of the first and second layer of each leg, respectively. The volume of the conductor  $V_w$  can be expressed as  $V_w = l_w A_{ws}$ , where  $A_{ws}$  is the single turn cross-section area.

## 4.7 Air-gap calculation

In the design process, the required inductance  $L$  and the peak flux density  $B_{pk}$  are basically functions of two variables, i.e. the number of turns  $N$  and air-gap length  $l_{ag}$ . Thus, the calculation of the air-gap is essential for the design. Air-gap calculation can be implemented using the magnetic circuit model.

A magnetic circuit model of an inductor enables a fast and simple inductance calculation. The inductance of an inductor with  $N$  winding turns and a total magnetic reluctance  $\mathcal{R}_{eq}$  is calculated as

$$L = \frac{N^2}{\mathcal{R}_{eq}} \quad (4.10)$$

Hence, the reluctances of the each section of the core and the air-gap have to be derived first in order to calculate the total reluctance. The calculation of the reluctances of the each section of core can be simply calculated using (3.8).

### 4.7.1 Magnetic circuit without fringing flux

Under the assumption of a homogeneous flux density distribution in the air gap and with no fringing flux, the air gap reluctance can be calculated using equation (3.9), where the area of the core cross section and the area of the air-gap are equal to each other. C-cut core configuration (cf. Fig. 4.4) consists of two air-gaps and two equal length of c-cut cores. The equivalent magnetic circuit is illustrated in Fig. 4.5. From the equivalent magnetic circuit the equivalent reluctance can be expressed as

$$\mathcal{R}_{eq} = \mathcal{R}_c + 2\mathcal{R}_{ag} = \frac{l_c}{\mu_0 A_c} \left( \frac{1}{\mu_r} + \frac{2l_{ag}}{l_c} \right) \quad (4.11)$$

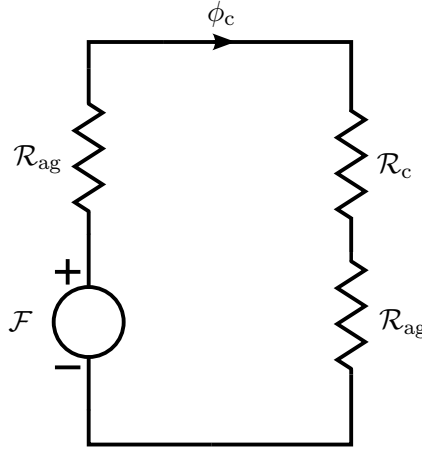


Figure 4.5: Equivalent magnetic circuit of the c-cut core configuration without fringing effect.  $\mathcal{R}_c$  defines the total reluctance of the core.

For the adjustment of the inductance  $L$ , the air-gap length of each leg  $l_{\text{ag}}$  can be obtained from the following equation

$$l_{\text{ag}} = \frac{N^2 \mu_0 A_c}{2L} - \frac{l_c}{2\mu_r} \quad (4.12)$$

where  $l_c$  is the core mean magnetic path length,  $\mu_0$  and  $\mu_r$  are the free-space and relative permeabilities, respectively. Fig. 4.8 shows the variation of the inductance (solid line) with respect to the air-gap length considering homogeneous flux density distribution using the AMCC016B core with  $B_{\text{pk}} = 1.25$  T,  $N = 56$  and  $\mu_r = 5000$ .

#### 4.7.2 Magnetic circuit with fringing flux

Equation (3.9) is only accurate when the air-gap length is very small compared to the dimension of the air-gap cross-section and the fringing flux is less compared to the total flux passing through the core. Thus, the fringing flux should be taken into consideration when designing an inductor to get the actual air-gap length and the corresponding inductance. Considering Fig. 3.6(b), the magnetic equivalent circuit for the c-cut core inductor including the fringing flux  $\phi_f$  is illustrated in Fig. 4.6. Considering the reluctance  $\mathcal{R}_f$  due to the fringing flux, the equivalent reluctance of the circuit with the fringing effect  $\mathcal{R}_{\text{eq},f}$  becomes

$$\mathcal{R}_{\text{eq},f} = \mathcal{R}_c + 2(\mathcal{R}_{\text{ag}} \parallel \mathcal{R}_f) \quad (4.13)$$

The maximum increase of each dimension of the core cross-section due to the fringing effect is approximately equal to the length of the air-gap [17]. Hence, the ratio of the effective width of the fringing flux cross-section area to the air-gap length is  $u = w_f/l_{\text{ag}}$  and the ratio of the effective magnetic path length of the fringing flux to

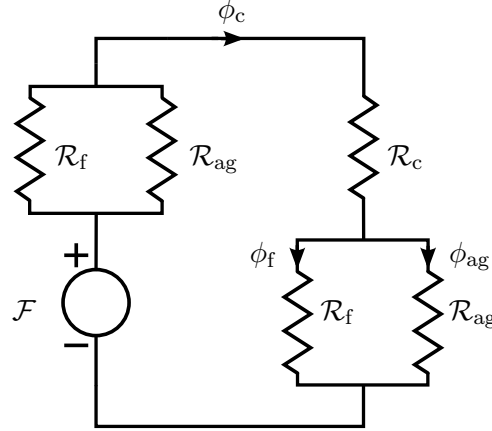


Figure 4.6: Equivalent magnetic circuit of the c-cut core configuration with fringing effect.  $\mathcal{R}_c$  defines the total reluctance of the core.

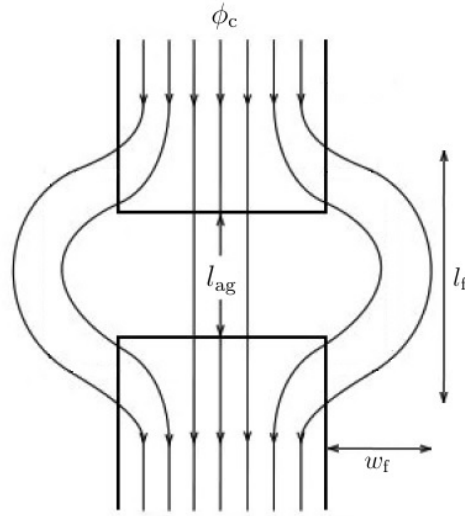


Figure 4.7: The relationship between the air-gap length, effective magnetic path length in the fringing flux and effective width of the fringing flux cross-section area [20].

the air-gap length is  $k = l_f/l_{ag} = 2$  (cf. Fig. 4.7). The fringing flux factor  $F_f$  can be expressed as

$$F_f = 1 + \frac{A_f}{kA_c} \quad (4.14)$$

where  $A_f$  is the cross-section area of fringing flux. Considering the core cross-sectional area from Fig. 4.4, the area of the fringing flux can be expressed as  $A_f = (A + 2ul_{ag})(D + 2ul_{ag}) - AD = 2ul_{ag}(A + D + 2ul_{ag})$ . Then, the fringing flux factor can be defined as

$$F_f = 1 + \frac{2ul_{ag}(A + D + 2ul_{ag})}{kAD} \quad (4.15)$$

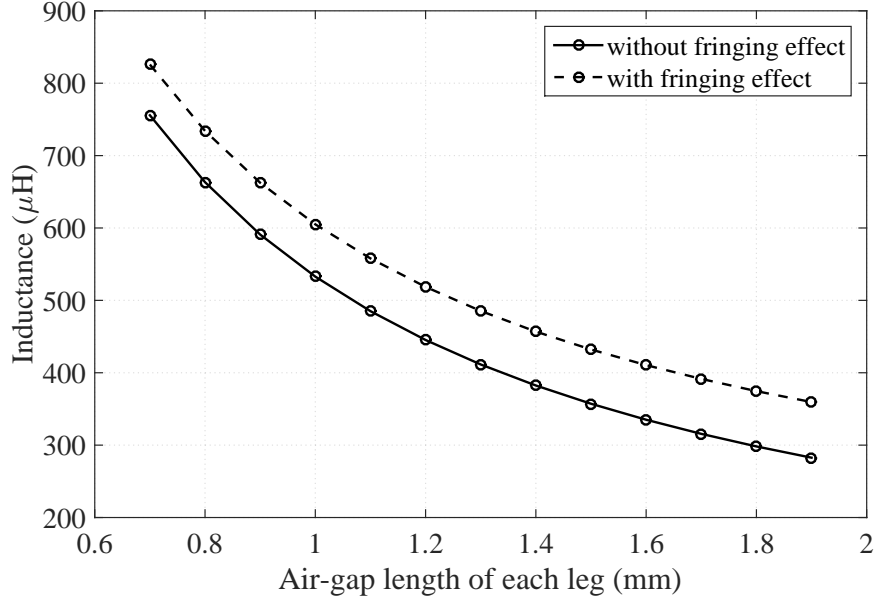


Figure 4.8: Variation of inductance due to change of air-gap length.

Under these assumptions, the equivalent reluctance of the circuit with the fringing effect  $\mathcal{R}_{\text{eq},f}$  can be solved from (4.13)

$$\mathcal{R}_{\text{eq},f} = \mathcal{R}_c + \frac{2\mathcal{R}_{\text{ag}}}{F_f} = \frac{l_{\text{ag}}}{\mu_0 A_c} \left( \frac{l_c}{\mu_r l_{\text{ag}}} + \frac{2}{F_f} \right) \quad (4.16)$$

For the adjustment of the required inductance  $L$  considering the fringing flux factor  $F_f$ , the new air-gap length  $l_{\text{ag}}$  is

$$l_{\text{ag}} = \frac{\mu_0 A_c F_f}{2L} \left( N^2 - \frac{L l_c}{\mu_r \mu_0 A_c} \right) \quad (4.17)$$

Iterative calculations are performed between (4.15) and (4.17) until both air-gap length  $l_{\text{ag}}$  and fringing factor  $F_f$  are converged. Finally, the estimated value of inductance  $L$  has to be verified using the values from (4.15) and (4.17) with the following equation

$$L_{\text{cal}} = \frac{\mu_0 A_c N^2}{l_c / \mu_r + 2l_{\text{ag}} / F_f} \quad (4.18)$$

Fig. 4.8 shows the variation of the inductance (dot-line) with respect to the air-gap length considering the fringing flux using the AMCC016B core with  $B_{\text{pk}} = 1.25$  T,  $N = 56$  and  $\mu_r = 5000$ . For obtaining the desired inductance with the same number of turns  $N$ , the air-gap length  $l_{\text{ag}}$  has to be increased.

## 4.8 Winding arrangements

For the c-cut cores shown in Fig. 4.4, each leg of the inductor comprises winding with  $N/2$  turns. The windings are rounded up in such a way that the second layer of

each leg don't overlap each other. At the first leg, the outer layer turns are rounded up at the lower side and at the second leg, the outer layer turns are rounded up at the upper side. Moreover, the windings of each leg are connected in series in such a way that the produced flux due to all windings are additive.

## 4.9 Loss calculation

Once the core area, area product, number of turns, and air-gap length are determined, the winding, core, and gap losses of the inductor are calculated.

### 4.9.1 Winding loss

The low frequency winding resistance, which is almost equal to dc winding resistance  $R_{w(dc)}$ , can be expressed as

$$R_{w(dc)} = \frac{\rho_w l_w}{A_w} \quad (4.19)$$

where,  $\rho_w = 17.24 \cdot 10^{-9} \Omega\text{m}$  is the electrical resistivity of the copper wire. The area of bare copper wire  $A_w$  and the length of the winding wire  $l_w$  can be calculated using (4.5) and (4.9), respectively. Dc winding power loss without the skin and proximity effects can be calculated using  $P_{w(dc)} = I_{rms}^2 R_{w(dc)}$ . The winding resistance of an inductor increases with the frequency because of the skin and proximity effects due to time-varying electromagnetic field. These two combined effects reduce the effective cross-section area of the winding available for the current flow. Thus, the ac winding resistance  $R_{w(ac)}$  at high frequencies becomes greater than the dc winding resistance  $R_{w(dc)}$ . The ac winding resistance of an inductor with  $N_l$  layers was derived by P. L. Dowell in [36] and presented in [14]. According to [14], the winding ac-to-dc resistance ratio can be expressed as

$$F_R = A_o \left( \frac{e^{2A_o} - e^{-2A_o} + 2 \sin(2A_o)}{e^{2A_o} + e^{-2A_o} - 2 \cos(2A_o)} + \frac{2(N_l^2 - 1)}{3} \frac{e^{A_o} - e^{-A_o} - 2 \sin A_o}{e^{A_o} + e^{-A_o} + 2 \cos A_o} \right) \quad (4.20)$$

where  $A_o$  is a dimensionless quantity which depends on conductor geometry. The skin and proximity effect contributions to the ac winding resistance are represented by the first and second term of (4.20), respectively. The factor of Dowell's equation for a round wire with diameter  $d$  is

$$A_o = \left( \frac{\pi}{4} \right)^{\frac{3}{4}} \frac{d}{\delta_w} \sqrt{\frac{d}{p}} \quad (4.21)$$

where  $p$  is the distance between the centres of two adjacent conductors and  $\delta_w$  is the skin depth of the conductor expressed as

$$\delta_w = \sqrt{\frac{\rho_w}{\pi \mu_0 \mu_{rw} f}} \quad (4.22)$$

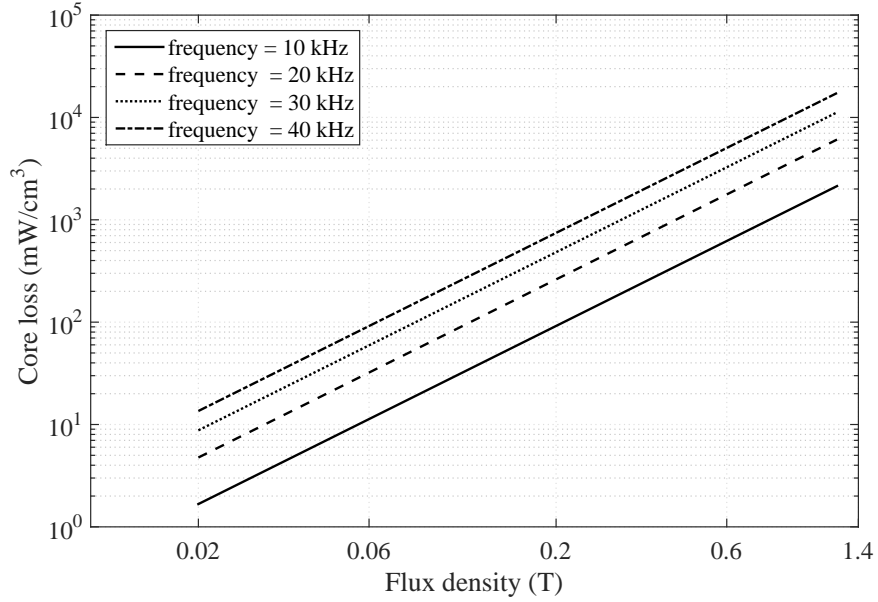


Figure 4.9: Core loss per unit volume versus the flux density amplitude for Fe-based amorphous core.

where  $\mu_{\text{rw}} = 1$  is the wire relative magnetic permeability, and  $f$  is the operating frequency. The high frequency ac winding resistance is expressed as  $R_{\text{w(ac)}} = F_{\text{R}} R_{\text{w(dc)}}$ . Finally, the high frequency ac winding power loss  $P_{\text{w}}$  can be obtained from

$$P_{\text{w}} = F_{\text{R}} P_{\text{w(dc)}} \quad (4.23)$$

#### 4.9.2 Core loss

Hysteresis losses, eddy current losses, and residual losses are the physical loss sources for the core material. The most used equation for characterizing the core losses  $p_{\text{v}}$  is the empirical power equation

$$p_{\text{v}} = k f^{\alpha} B_{\text{pk}}^{\beta} \quad (4.24)$$

where  $B_{\text{pk}}$  is the peak flux density amplitude of a sinusoidal excitation with frequency  $f$ , and  $k$ ,  $\alpha$ ,  $\beta$  are the material parameters referred to as the Steinmetz parameters [17, 28]. The equation is called the Steinmetz equation (SE). Core manufacturers provide the data of core losses per unit volume as a function of frequency  $f$ , and peak flux density  $B_{\text{pk}}$ . Fig. 4.9 shows (4.24) considering the amorphous core with the parameters  $k = 6.5$ ,  $\alpha = 1.51$ , and  $\beta = 1.74$ .

The basic empirical SE predicts specific core losses for sinusoidal flux waveforms with good accuracy. However, the SE is not capable of accurately calculating core losses for non-sinusoidal flux waveforms in power electronic applications. To overcome this limitation, different approaches have been developed. The modified formula of the Steinmetz equation (MSE) over nonsinusoidal waveforms is presented in [37] by

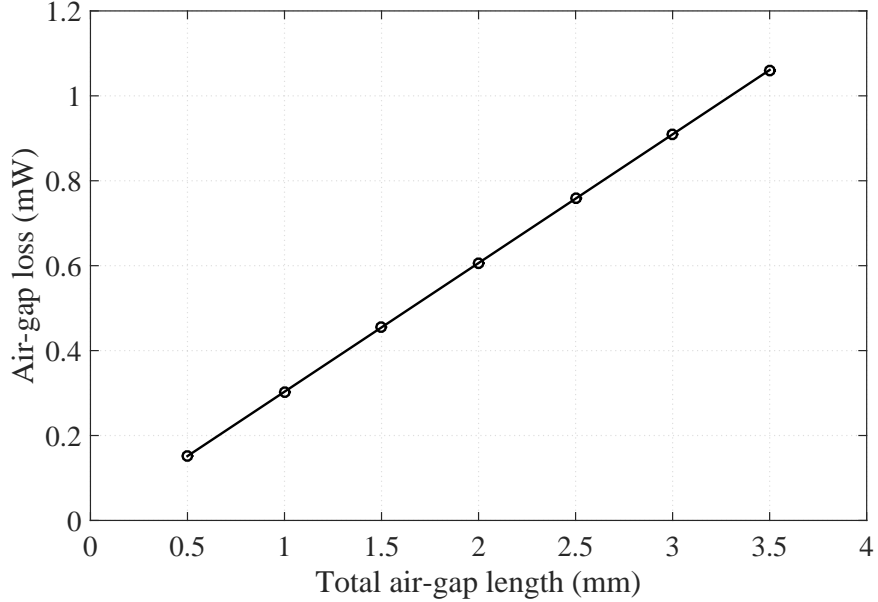


Figure 4.10: Air-gap loss in the inductor.

replacing  $f$  with remagnetization rate  $dM/dt$ , which is proportional to the rate of change of induction  $dB/dt$ . The improved generalized Steinmetz equation (iGSE) is introduced in [38] dealing with minor hysteresis loops. The improved-improved generalized Steinmetz equation ( $i^2$ GSE) is suggested in [39] to solve the problem of different flux shapes. Once the core loss per unit volume is calculated, the total core loss can be calculated from

$$P_c = p_v V_c \quad (4.25)$$

where  $V_c$  is the volume of the core material. The volume of the core material can be expressed with the core mean magnetic path length  $l_c$  and the core cross-section  $A_c$  as  $V_c = l_c A_c$ , where the core mean magnetic path length can be obtained from  $l_c = 2(B + C) + \pi A$ .

#### 4.9.3 Air-gap loss

Magnetic materials can have additional eddy-current core losses due to the air-gap fringing flux. These core losses are caused by the magnetic fringing flux around the gap reentering the core. Some of the fringing flux strike the core perpendicular to the laminations due to the increase of the air-gap length. The nominal air-gap loss  $P_{ag}$  can be expressed as [19]

$$P_{ag} = k_i w_l l_{ag,t} f B_{pk}^2 \quad (4.26)$$

where  $k_i$  is the core constant (e.g. 0.388 for a pair of c-cut core),  $w_l$  is the lamination width,  $l_{ag,t}$  is the total air-gap length. The total air-gap loss in the inductor is shown in Fig. 4.10 for the frequency of 20 kHz and the peak flux density of 1.25 T. The

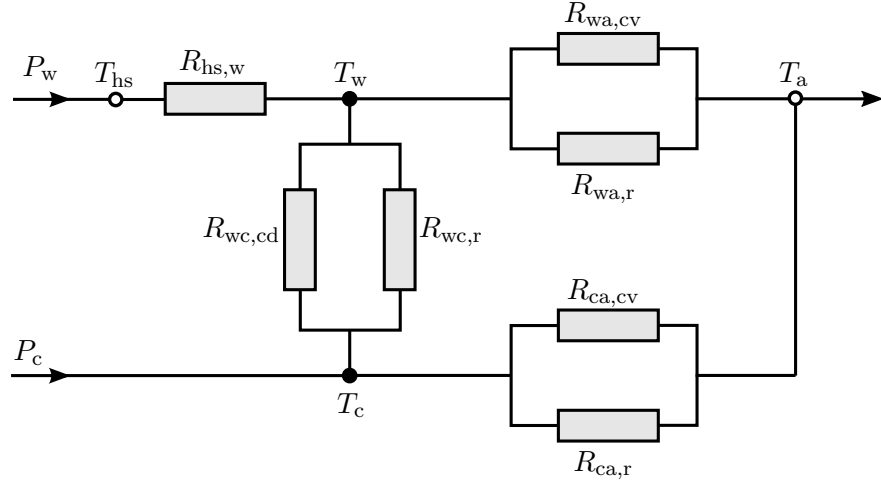


Figure 4.11: Thermal equivalent circuit of an inductor when the hotspot is on the windings.

leakage flux in the vicinity of the gap increases as the air-gap length increases. Thus, the core loss due to this leakage flux also increases. However, the air-gap loss is negligible compared to the total core loss.

#### 4.9.4 Total power loss

Once the winding loss  $P_w$  and the core loss  $P_c$  are determined, the total power loss in the inductor  $P_t$  can be calculated from

$$P_t = P_w + P_c \quad (4.27)$$

### 4.10 Thermal modeling

The losses generated in the winding and in the core give rise to the heating. The heat transfer rate  $q$  is equal to the total power loss  $P_t$  of the inductor [12, 27]. The temperature rise  $\Delta T$  is the difference between the temperature of the hot-spot  $T_{hs}$  in the inductor and the ambient temperature  $T_a$ . The temperature rise can be expressed as  $\Delta T = P_t R_{th}$ , where  $R_{th}$  is the total thermal resistance of the inductor.

To obtain the temperature rises in each part of the inductor, the thermal equivalent circuit is needed. Fig. 4.11 shows the inductor thermal equivalent circuit when the hot-spot is on the windings [27]. The thermal model contains all types of heat transfers represented by equivalent thermal resistances. In the circuit,  $R_{hs,w}$  represents the conduction thermal resistance of the conductor. The combination of the conduction thermal resistance  $R_{wc,cd}$  and the radiation thermal resistance  $R_{wc,r}$  between the conductor surface and the core is represented by the thermal resistance  $R_{wc}$ . The thermal resistance between the core and the ambient  $R_{ca}$  is based on the radiation thermal resistance  $R_{ca,r}$  and the convection thermal resistance  $R_{ca,rv}$ . The thermal

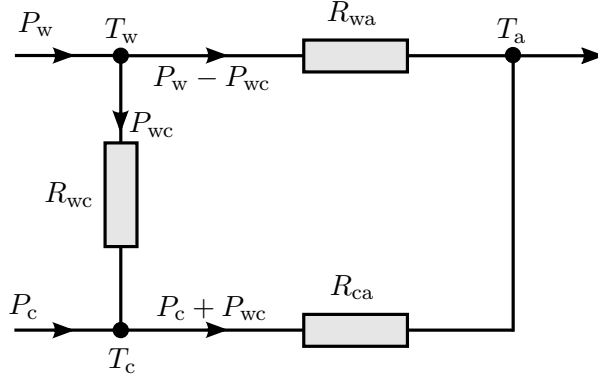


Figure 4.12: Simplified thermal circuit of an inductor.

resistance between the conductor and the ambient  $R_{wa}$  is the combination of the convection thermal resistance  $R_{wa, cv}$  and the radiation thermal resistance  $R_{wa, r}$ .  $T_w$ ,  $T_c$ , and  $T_a$  represent the temperatures of the conductor surface, the core surface, and the ambient temperature, respectively. The ambient temperature is assumed to be constant at 20 °C.

The conduction thermal resistance between the conductor surface and the core is expressed as  $R_{wc,cd} = l_{wc}/k_{ta}A_{wc}$ , where  $l_{wc}$  is the equivalent air-gap corresponding to the air space between the conductor and the core,  $A_{wc}$  is the surface realizing the conduction between the conductor and the core, and  $k_{ta} = 0.031 \text{ W/mK}$  is the air thermal conductivity [27]. The radiation thermal resistances can be obtained using the Stefan-Boltzmann law of thermal radiation

$$R_{wc,r} = \frac{T_w - T_c}{\sigma \varepsilon_w (T_w^4 - T_c^4) A_{wc}} \quad (4.28a)$$

$$R_{wa,r} = \frac{T_w - T_a}{\sigma \varepsilon_w (T_w^4 - T_a^4) A_{wa}} \quad (4.28b)$$

$$R_{ca,r} = \frac{T_c - T_a}{\sigma \varepsilon_c (T_c^4 - T_a^4) A_{ca}} \quad (4.28c)$$

where  $\varepsilon_w = 0.8$  and  $\varepsilon_c = 0.9 - 0.95$  are the emissivity of conductor and core surfaces, respectively [27].  $\sigma = 5.67 \cdot 10^{-8} \text{ W/m}^2\text{K}^4$  is the Stefan-Boltzmann constant.  $A_{wa}$  and  $A_{ca}$  are the conductor and the core open surfaces, respectively that transfer heat directly to the ambient air. The convection thermal resistances are expressed using the Newton law of cooling

$$R_{wa, cv} = \frac{1}{h_c A_{wa}} \quad (4.29a)$$

$$R_{ca, cv} = \frac{1}{h_c A_{ca}} \quad (4.29b)$$

where  $h_c$  is the convection heat transfer coefficient of the material. For natural convection cooling, the convection heat transfer coefficient can be expressed as  $h_c = 1.42 (\Delta T/H_v)^{0.25}$ , where  $H_v$  is the vertical height of the component. For the forced

convection with the air velocity of  $v$ , the convection heat transfer coefficient can be defined as  $h_c = (3.33 + 4.8v^{0.8})/H_t^{0.288}$ , where  $H_t$  is the total length of the boundary layer of the component [27].

The conduction thermal resistance  $R_{hs,w}$  can be short-circuited due to high thermal conductivity of the winding materials [40]. The thermal conductivity of the copper winding is 379 W/mK [27]. In the design, it is assumed that all copper surfaces have the same temperature and all core surfaces also have the same temperature. The simplified equivalent circuit is shown in Fig. 4.12.  $P_{wc}$ ,  $P_w - P_{wc}$ , and  $P_c + P_{wc}$  represent the power dissipations between the conductor-to-core, the conductor-to-ambient, and the core-to-ambient, respectively. Applying the circuit theory in Fig. 4.12, the following equations can be written

$$\Delta T = T_w - T_a = (P_w - P_{wc})R_{wa} \quad (4.30)$$

$$(P_w - P_{wc})R_{wa} = P_{wc}R_{wc} + (P_c + P_{wc})R_{ca} \quad (4.31)$$

Solving (4.31) for the power dissipations between the conductor-to-core

$$P_{wc} = \frac{P_w R_{wa} - P_c R_{ca}}{R_{wc} + R_{wa} + R_{ca}} \quad (4.32)$$

Substituting (4.32) into (4.30), for the given values of the winding and core losses, the temperature rise of the inductor becomes

$$\Delta T = \left( \frac{P_w R_{wc} + P_w R_{ca} + P_c R_{ca}}{R_{wc} + R_{wa} + R_{ca}} \right) R_{wa} \quad (4.33)$$

All open surfaces of an inductor are assumed to have same temperature in an isotherm surface model [27]. Then, the total heat transfer rate can be expressed as  $q = q_{cd} + q_r + q_{cv}$ , where  $q_{cd}$ ,  $q_r$ , and  $q_{cv}$  are the conduction, the radiation, and the convection heat transfer rate, respectively. Using the heat transfer laws, the total heat transfer rate can be defined as

$$q = k_{tc} A_c \frac{T_w - T_a}{l_c} + \sigma \varepsilon A_r (T_w^4 - T_a^4) + h_c A_{cv} (T_w - T_a) \quad (4.34)$$

where  $k_{tc}$  is the thermal conductivity of the core material,  $A_r$  and  $A_{cv}$  are the radiating and convecting area of the component [27]. Equation (4.34) gives the rough estimate about the percentage of heat transfer rate by the conduction, the radiation, and the convection process.

The aforementioned explained design procedure in section 4 have to be satisfied with the design constraints of the inductor. The obtained parameters using the design algorithm are given in the next section.

# 5 Results

The area product method, which is explained in section 4, is used to design the inductor for the LCL filter. The design algorithm is implemented for natural and air-forced cooling conditions. This section describes the obtained results from the designed inductors. Finally, the experimental results for the prototype inductor are presented.

The optimized value of the converter-side inductance is  $350 \mu\text{H}$ . To implement the design algorithm, the specifications from section 2.3 are used together with the waveform in Fig. 2.3. The algorithm is implemented using a MATLAB script given in the Appendix. The inductor is designed with a single-wire winding using a gapped core. The peak flux density  $B_{\text{pk}} = 0.8 \cdot B_{\text{sat}}$  is assumed and the considered window utilization factor is  $K_u = 0.4$ .

## 5.1 Design examples

From the comparison of different core materials in section 4.3.2, the Vitroperm500F and the 3C93 core materials result the largest inductor due to the low saturation flux density. The 10JNHF600 and Xflux core materials have higher core loss density. To avoid overheating, the core losses should be kept low. Thus, the preferred option is the 2605SA1 core material under natural cooling condition.

Since the air-forced cooling removes the produced heat more efficiently than the natural convection cooling, all materials are limited by the saturation flux density under the air-forced convection cooling. As can be seen from Fig. 4.3, the 2605SA1 and the 10JNHF600 core materials are competitive. Therefore, the design algorithm is implemented using the 2605SA1 and the 10JNHF600 core materials and the results are compared.

Table 5.1: Specifications of the AMCC0025 core material [41].

| Symbol | Parameter                                  | Value  |
|--------|--|--------|
| $A_c$  | Core cross-section area ( $\text{mm}^2$ )  | 325    |
| $W_a$  | Core window area ( $\text{mm}^2$ )         | 840    |
| $l_c$  | Core magnetic path length (mm)             | 194    |
| $V_c$  | Volume of the core ( $\text{mm}^3$ )       | 63050  |
| $A_p$  | Area product of the core ( $\text{mm}^4$ ) | 273000 |

Table 5.2: Specifications of the copper wire used for natural cooling [35].

| Symbol | Parameter                                | Value |
|--------|--|-------|
| $d$    | Nominal conductor diameter (mm)          | 2.8   |
| $d_o$  | Nominal outer diameter (mm)              | 2.92  |
| $A_w$  | Area of bare conductor ( $\text{mm}^2$ ) | 6.158 |

### 5.1.1 Design example 1: Natural cooling (Amorphous core)

The initial rms current density  $J_m = 3 \text{ A/mm}^2$  is assumed under natural cooling. The peak flux density is considered to be 1.25 T for the 2605SA1 core material. The calculated rms current density is 2.97 A/mm<sup>2</sup> and the calculated area product is  $A_{p,\text{cal}} = 186557 \text{ mm}^4$ . The inductor is designed using the AMCC0025 core and the IEC 60317-0-1 standard copper wire. The specifications of the AMCC0025 core and the copper wire are given in Table 5.1 and Table 5.2, respectively. The Steinmetz equation parameters are  $k = 6.5$ ,  $\alpha = 1.51$ , and  $\beta = 1.74$  for the 2605SA1 core material [41]. The core fill factor is  $k_c = 0.82$  and the core density is 7.18 g/cm<sup>3</sup> [19].

For the required inductance and to satisfy the peak flux density, 30 turns are required. The calculated length of the winding is  $l_w = 2520 \text{ mm}$ . The estimated length of the air-gap is  $l_{\text{ag}} = 0.54 \text{ mm}$  and the calculated fringing flux factor is  $F_f = 1.06$ . The dc and ac winding resistances are 7.1 mΩ and 36.8 mΩ, respectively. The total winding loss is  $P_w = 12.31 \text{ W}$  and the core loss is  $P_c = 5.17 \text{ W}$ . The total mass of the inductor is  $m_i = 530 \text{ g}$  and the final volume is  $V_i = 79925 \text{ mm}^3$ .

### 5.1.2 Design example 2: Air-forced cooling (Amorphous core)

It is assumed that the initial rms current density is 6 A/mm<sup>2</sup> under air-forced convection cooling. The calculated rms current density is 5.82 A/mm<sup>2</sup> and the calculated area product is  $A_{p,\text{cal}} = 95187 \text{ mm}^4$ . The calculated area product satisfies the AMCC0010 core. The inductor is designed using the IEC 60317-0-1 standard copper wire. Table 5.3 gives the specifications of the AMCC0010 core. The specifications of the copper wire under air-forced cooling is given in Table 5.4.

The number of turns  $N = 44$  is required to satisfy the required peak flux density

Table 5.3: Specifications of the AMCC0010 core material [41].

| Symbol | Parameter                                  | Value  |
|--------|--|--------|
| $A_c$  | Core cross-section area ( $\text{mm}^2$ )  | 220    |
| $W_a$  | Core window area ( $\text{mm}^2$ )         | 520    |
| $l_c$  | Core magnetic path length (mm)             | 150    |
| $V_c$  | Volume of the core ( $\text{mm}^3$ )       | 33000  |
| $A_p$  | Area product of the core ( $\text{mm}^4$ ) | 114400 |

Table 5.4: Specifications of the copper wire used for air-forced cooling [35].

| Symbol | Parameter                                | Value |
|--------|--|-------|
| $d$    | Nominal conductor diameter (mm)          | 2.0   |
| $d_o$  | Nominal outer diameter (mm)              | 2.11  |
| $A_w$  | Area of bare conductor ( $\text{mm}^2$ ) | 3.14  |

and to obtain the required inductance. Using AMCC0010 core, maximum 15 turns per layer can be fitted. The total length of the winding is  $l_w = 3198$  mm. The calculated length of the air-gap is  $l_{ag} = 0.86$  mm and the fringing flux factor is  $F_f = 1.13$ .

The dc resistance is 17.5 mΩ and the corresponding winding loss is 5.87 W. Considering the skin and proximity effect at 20 kHz, the total winding resistance is 124.4 mΩ. Thus, the final winding loss is  $P_w = 41.67$  W. The total core loss is  $P_c = 2.74$  W. The core loss of the 50 Hz component is 25 mW and the core loss due to the ripple component is 2.71 W. The final mass of the inductor is  $m_i = 298$  g and the final volume is  $V_i = 44204$  mm<sup>3</sup>.

### 5.1.3 Design example 3: Air-forced cooling (JNHF core)

It can be seen from Fig. 4.4 that the dimensions of the geometric parameters can be varied to perform a design of an inductor. Moreover, the width of the 10JNHF600 core material strip varies up to 600 mm [42]. Therefore, the inductor can be designed using the 10JNHF600 material with user defined core dimensions. The saturation flux density of the 10JNHF600 core material is  $B_{sat} = 1.88$  T, the core fill factor is  $k_c = 0.90$ , and the density of the core material is 7.53 g/cm<sup>3</sup> [42]. Using the curve fitting from the data given in [42], the obtained Steinmetz's equation parameters are  $k = 2.14 \cdot 10^{-3}$ ,  $\alpha = 1.384$ , and  $\beta = 1.981$  for the 10JNHF600 core material.

The peak flux density of 1.50 T is considered in this case. The inductor is designed using the same rms current density and the same copper wire like the design example in section 5.1.2. The calculated area product is  $A_{p,cal} = 78985$  mm<sup>4</sup>. Hence, the AMCC0008 core dimensions are considered as the references. The dimensions of the used 10JNHF600 core are as follows: core width  $A = 11$  mm, window width  $B = 15$

Table 5.5: Specifications of the used 10JNHF600 core material.

| Symbol | Parameter                                  | Value |
|--------|--|-------|
| $A_c$  | Core cross-section area ( $\text{mm}^2$ )  | 220   |
| $W_a$  | Core window area ( $\text{mm}^2$ )         | 450   |
| $l_c$  | Core magnetic path length (mm)             | 130   |
| $V_c$  | Volume of the core ( $\text{mm}^3$ )       | 28600 |
| $A_p$  | Area product of the core ( $\text{mm}^4$ ) | 99000 |

mm, window length  $C = 30$  mm, and core height  $D = 20$  mm. To simplify the design, only the window width  $B$  has been changed. Table 5.5 gives the specifications of the used 10JNHF600 core material.

The number of turns  $N = 33$  is required to satisfy the required inductance and the peak flux density. The total length of the winding is  $l_w = 2481$  mm. The estimated air-gap length is  $l_{ag} = 0.42$  mm and the fringing flux factor is  $F_f = 1.06$ . The dc resistance of the winding is  $13.6 \text{ m}\Omega$ . The final winding resistance at 20 kHz is  $96.5 \text{ m}\Omega$  and the corresponding winding loss is  $P_w = 32.33 \text{ W}$ . The total core loss  $P_c = 6.54 \text{ W}$  is the combination of the core loss due to the fundamental component of 230 mW and the core loss of the ripple component of 6.31 W. Finally, the total loss of the inductor is 38.87 W, the total mass is 293 g, and the final volume of the inductor is 37293  $\text{mm}^3$ .

#### 5.1.4 Discussion

It can be seen from the results that the area product of the inductor is reduced by 50% if the air-forced cooling condition is considered with the same core material of the 2605SA1. The total volume of the inductor under air-forced cooling is 55% of the inductor with natural cooling. However, the total loss is increased in air-forced cooling condition due to the higher winding resistance.

A conventional filter with the inductance of 2.94 mH on the converter side is used in [24] with a grid-connected converter having the air-forced cooling with the air-velocity of 6.72 m/s. The dimensions of the conventional inductor are as follows: core width  $A = 20$  mm, window width  $B = 20$  mm, window length  $C = 60$  mm, and core height  $D = 30$  mm. The area product of the core is  $A_p = 720000 \text{ mm}^4$ . The inductor is designed in section 5.1.2 using the AMCC0010 core considering the same air-forced cooling condition in [24]. The obtained area product of the designed inductor is only 16% of the conventional inductor.

Since the peak flux density of the 10JNHF600 core material is 20% higher than that of the 2605SA1 core material, the calculated area product of the inductor using the 10JNHF600 core material is almost 20% lower in comparison with the inductor designed with the 2605SA1 core material at the rated operating point. Hence, the air-forced cooling with the same air-velocity of 6.72 m/s is considered.

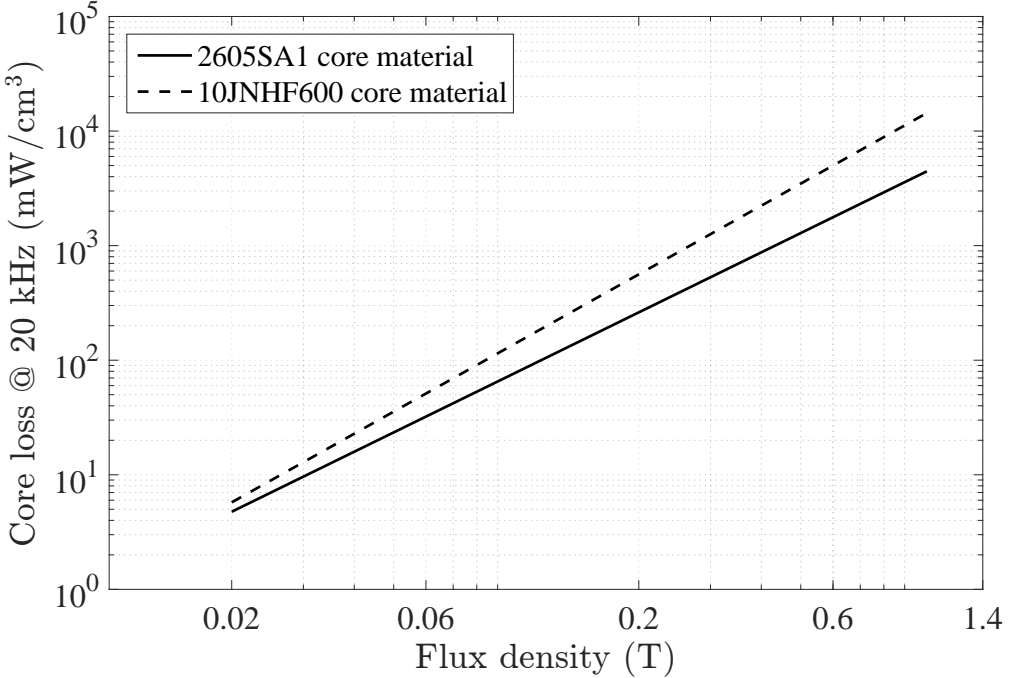


Figure 5.1: Core loss per unit volume versus flux density amplitude at 20 kHz.

The area product of the used 10JNHF600 core in section 5.1.3 is 86% of the area product of the AMCC0010 core. The calculated winding loss in the inductor with the 10JNHF600 core is 78% of the inductor with the AMCC0010 core. However, the core-loss density of the 10JNHF600 core material is higher than the core-loss density of the 2605SA1 core material. The differences of the core-loss densities increase with the flux density (cf. Fig. 5.1). According to the results, the core loss at 20 kHz with the 10JNHF600 core material is 2.38 times larger in comparison with the 2605SA1 core material. Finally, the overall volume of the inductor with the 10JNHF600 core material is about 84% of the inductor with the 2605SA1 core material. Fig. 5.2 shows the obtained area product and the volume of the core of the inductors with different core materials and cooling conditions.

Table 5.6 gives the thermal performances of the designed inductors using different core materials under natural and air-forced cooling conditions. In the designs, the calculated temperature rise varies between 70-80 °C. As can be seen from the results, the most of the heat is being transferred through convection process under air-forced cooling conditions. On the other hand, the inductor transfers heat equally through the radiation and the convection process under natural cooling condition. The conduction heat transfer rate varies between 2-7% of the total heat transfer rate. Since the temperature rise is inversely proportional to the heat radiating surface, the inductor with the 10JNHF600 core material generates more heat in comparison with the inductor with the 2605SA1 core material. However, the total losses in the inductor with the 10JNHF600 core material are only 87% of the losses with the 2605SA1 core material.

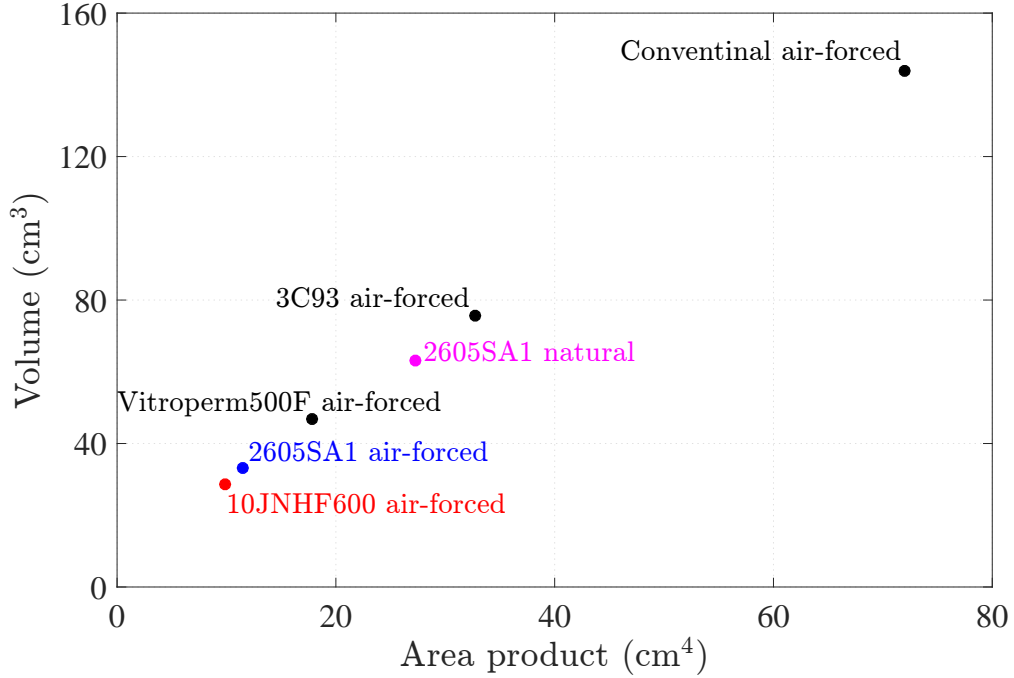


Figure 5.2: The area product versus the volume of the core of the inductors.

Table 5.6: Thermal performances of the inductors.

| Parameter                               | Natural | Air-forced | Air-forced |
|---|---------|------------|------------|
|   | 2605SA1 | 2605SA1    | 10JNHF600  |
| Temperature rise ( $^{\circ}\text{C}$ ) | 70      | 77         | 80         |
| Share of conduction heat transfer (%)   | 6.87    | 2.5        | 6.06       |
| Share of radiation heat transfer (%)    | 45.65   | 11.73      | 11.00      |
| Share of convection heat transfer (%)   | 47.48   | 85.77      | 82.90      |

The design is implemented in section 5.1.3 with the 10JNHF600 core material using user defined core dimensions. As can be seen from Fig. 5.2, a more compact inductor can be designed with the 10JNHF600 core material than with the 2605SA1 core material. However, the user defined core dimensions are difficult to line up and also not practical. Moreover, the 10JNHF600 core material is more costly in comparison with the 2605SA1 core material. Under these considerations, the 2605SA1 core material is selected for the final design. The designed inductor is manufactured using the 2605SA1 core material to be used in grid-connected converter under air-forced cooling condition.

## 5.2 Experiments

Fig. 5.3 shows the photographs of the manufactured prototype inductor. The tolerance of  $\pm 10\%$  was considered for the design by the manufacturer. Fig. 5.4(a) shows

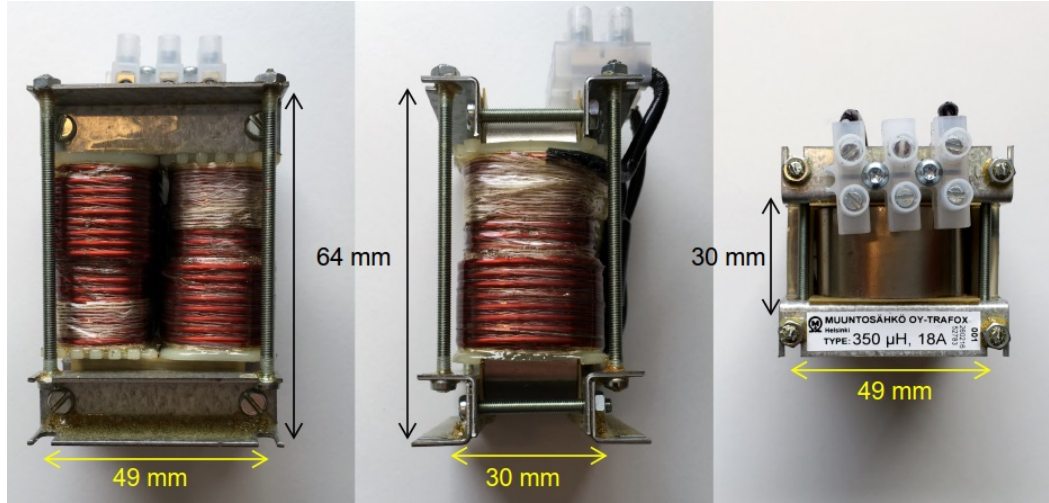


Figure 5.3: Prototype inductor: front-view, side-view, and top-view (from left).

the variation of the voltage and current from the voltage impulse test performed by the manufacturer. The variation of the inductance due to the change of the applied current into the inductor is shown in Fig. 5.4(b). The result shows that the inductor provides the inductance within  $\pm 10\%$  of the required value.

The prototype inductor is evaluated by means of laboratory experiments. The inductor is supplied with the current at the fundamental frequency of 50 Hz. The current through the inductor and the reactance are measured using a power analyzer. The measured inductance is  $379 \mu\text{H}$  at the rated operating point. Further, the current is varied from 0 A to 24 A to evaluate the flux linkage of the inductor. The relation between the current and the flux linkage of the inductor is shown in Fig. 5.5.

To observe the magnetization curve of the prototype inductor, the auxiliary winding is rounded up around the core. The supplied peak value of the fundamental current and the induced auxiliary winding voltage are measured. The calculated peak flux density (4.4) caused by the fundamental current is 1.13 T at the rated operating point. In the prototype inductor, the measured peak flux density due to the fundamental current is 1.07 T. Fig. 5.6 shows the measured peak flux density of the prototype inductor for different currents. The peak value of the saturation current of 40.15 A is required to reach the saturation peak flux density of 1.56 T.

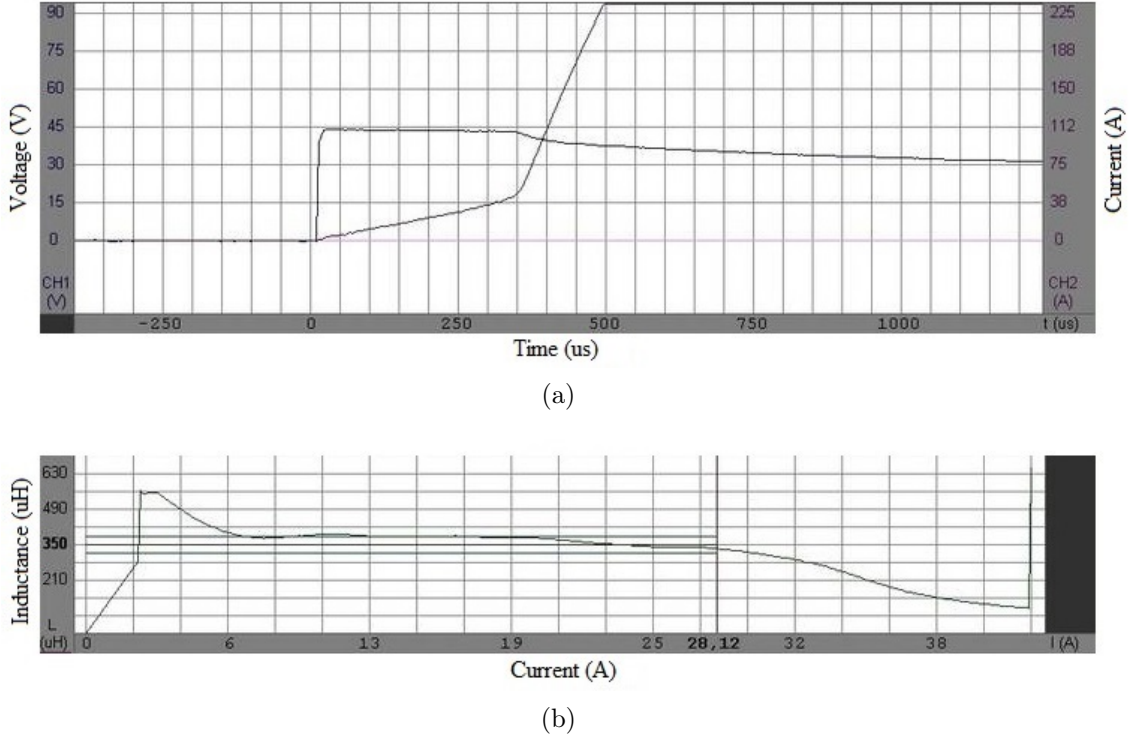


Figure 5.4: Inductor tests: (a) voltage impulse test of the prototype inductor; (b) variation of inductance due to change of current.

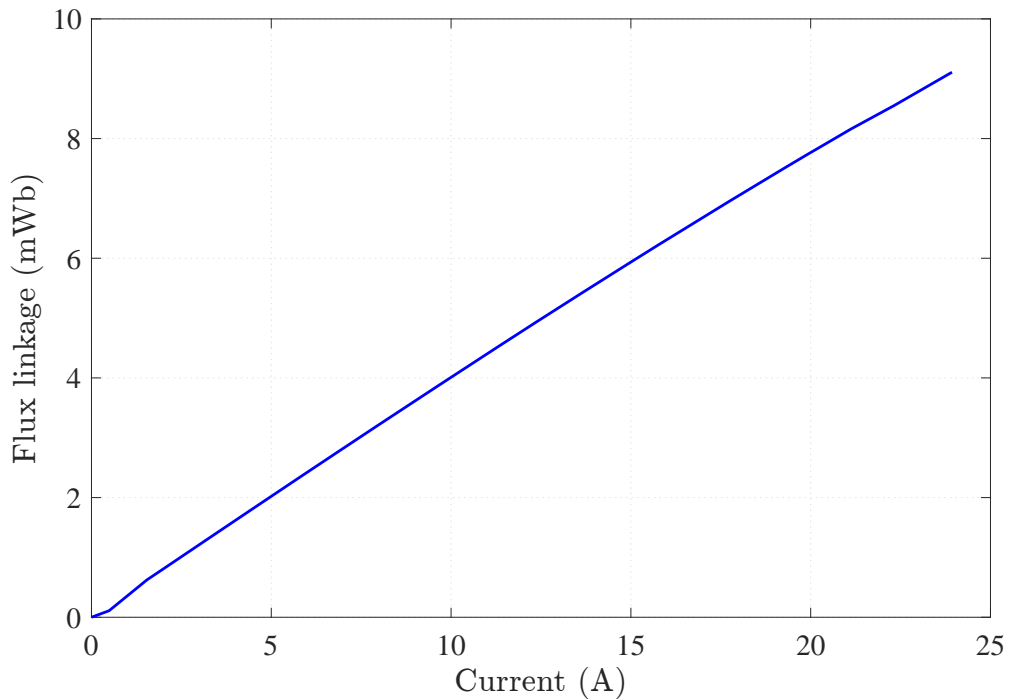


Figure 5.5: The flux linkage versus the current of the prototype inductor.

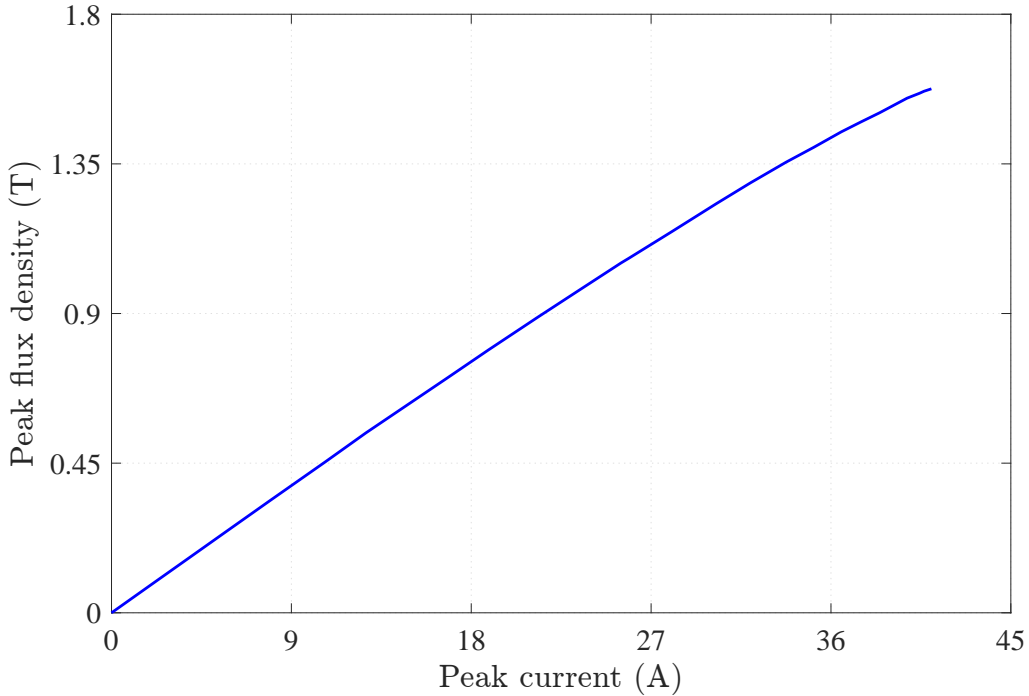


Figure 5.6: Variation of the peak flux density due to change of the applied peak current.

### Frequency responses

The frequency response of the prototype inductor is measured using a frequency response analyser (FRA) [43]. The FRA is employed to carry out the measurement for the frequency range from 10 Hz to 100 kHz. A sinusoidal signal of 1.0 V peak-to-peak is applied for the measurement. Fig. 5.7 shows the measured inductance of the prototype inductor as well as the constant inductance of  $379 \mu\text{H}$ . As can be seen, the designed inductor coincides the constant inductance up to 10 kHz. The measured inductance at 20 kHz is  $362 \mu\text{H}$ .

The measured impedance and the calculated impedance are shown in Fig. 5.8. The result shows that the measured high-frequency behaviour describes nearly the constant inductor in the whole examined frequency range. Fig. 5.9 shows the variation of the measured equivalent series resistance  $R_s$  and reactance  $X_s$  of the prototype inductor up to 100 kHz. The total ac resistance increases with the frequency due to the skin and proximity effects in the windings. The measured reactance follows the reactance of the constant inductance for the whole frequency range.

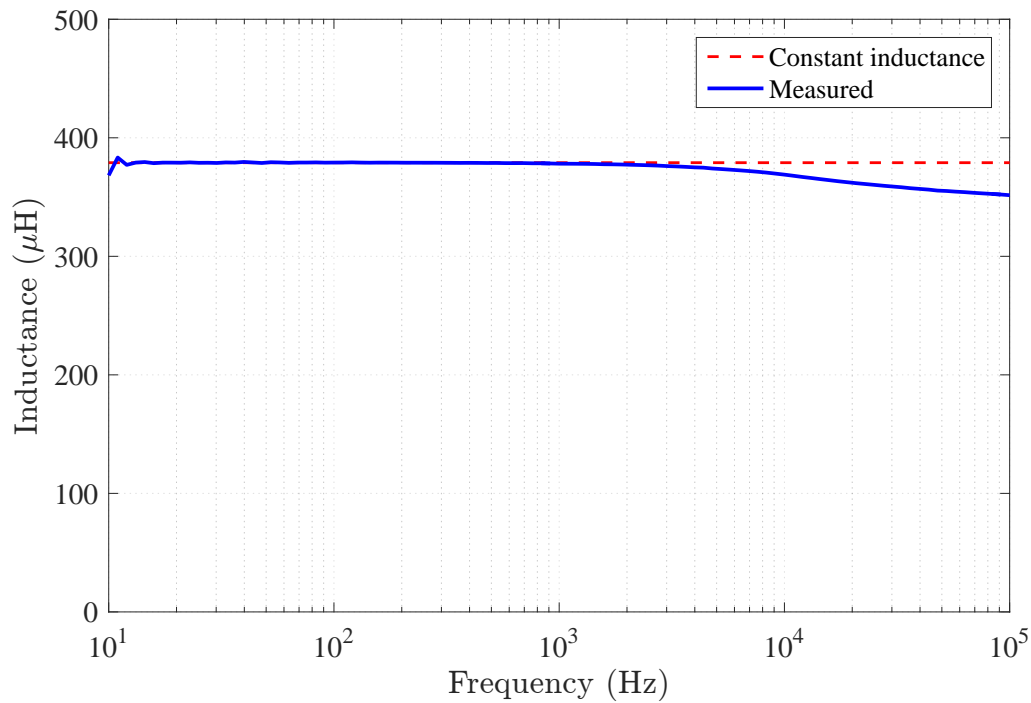


Figure 5.7: Measured and calculated inductance of the prototype inductor.

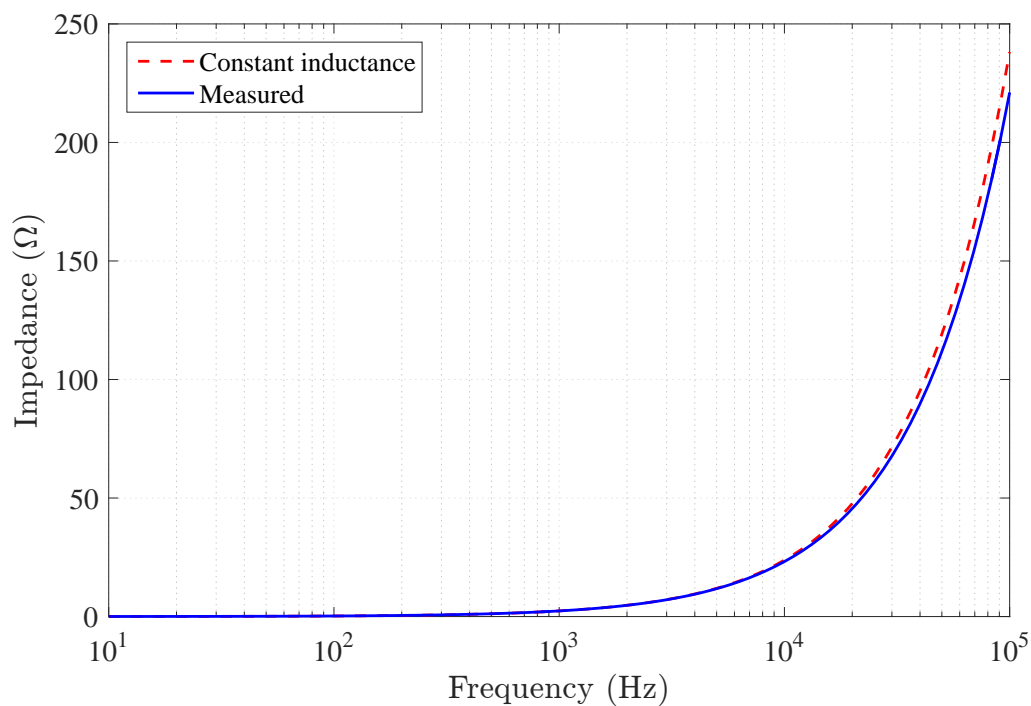


Figure 5.8: Measured and calculated impedance of the prototype inductor.

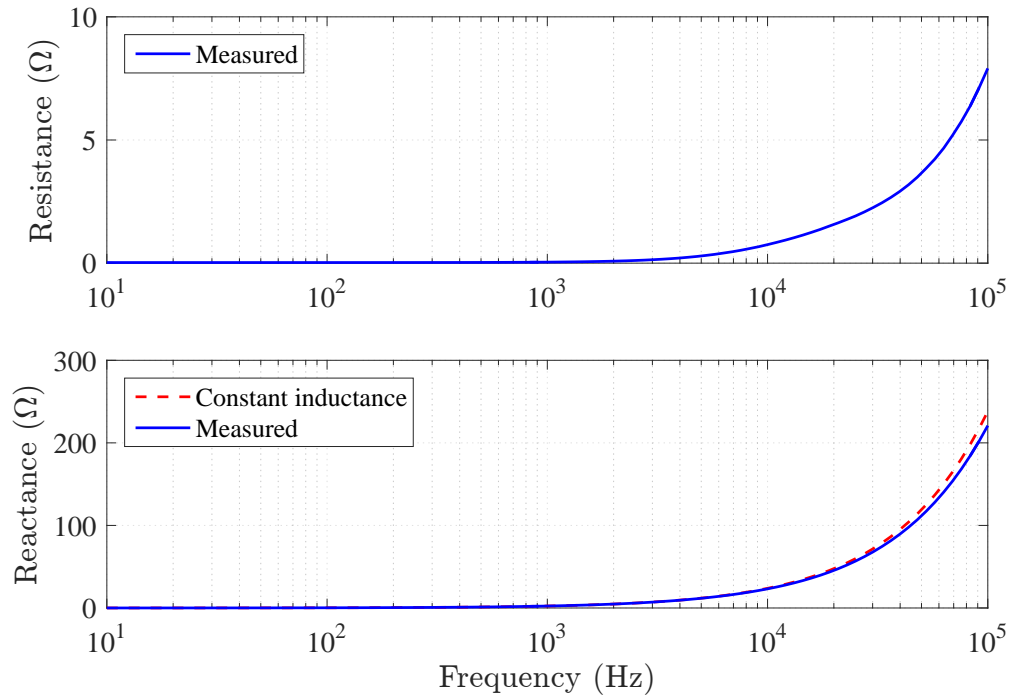


Figure 5.9: Measured equivalent series resistance  $R_s$  (upper figure) and the comparison of measured and calculated reactance  $X_s$  (lower figure).

## 6 Conclusions

In this thesis, a design procedure of an inductor used in grid-connected converters is presented. The compact design of a converter-side inductor of an LCL filter is implemented using the area product approach. Both the fundamental and switching frequency effects were considered to calculate the peak flux density. The core material was selected based on the peak flux density within the saturation and the core-loss density limits. Since the selection of the core material determines the area product of the inductor, special attention was given for the selection of the core material. Different core materials were analysed and investigated to get the optimum design.

Moreover, the optimal choice of the core dimensions was considered to reduce the size of the inductor. The core was selected based on the calculated area product value of the inductor. Since the losses of the inductor were not considered while reducing the volume, the heat transfer to the ambient was considered in order to limit the temperature rise. The winding wire was selected based on the value of the rms current density. The natural and air-forced cooling conditions were considered to select the proper size of the winding wire. The gapped core was considered for the design to increase the linear part of the magnetization curve. The required inductance was obtained by adjusting the length of the air-gap. In addition, the fringing flux factor was considered during the design and the effect of the fringing flux on the inductance was studied. The winding and core losses in the inductor were calculated based on the Dowell and Steinmetz equation, respectively. The air-gap loss in the inductor was neglected. The temperature rise due to the losses in the inductor was calculated to verify the design.

The design method gives an estimate of the size of the inductors used in the grid-connected converter. The design method was implemented on three different designs and the results were compared. The results show the effects of the peak flux density of the material on the size of the inductors. The larger value of the peak flux density gives reduced area product using the same cooling conditions. Further, the effects of the cooling conditions on the size of the inductors are discussed. The results show that the same core material provides lower area product under air-forced cooling

condition. Again, the reduced area product gives higher temperature rise even with the same cooling condition.

A prototype inductor was manufactured using the given design methodology. The prototype inductor was measured and compared with the obtained simulation results. The comparisons show that the calculated results are in good agreement with the measurements. The frequency responses show the effects of the frequency on the impedance of the inductor. The high-frequency behaviour follows the impedance of the constant inductance in the measured frequency range.

Overall, the objectives of the thesis are achieved. The size of the inductor is decreased significantly by selecting higher value of the peak flux density and using air-forced cooling condition. In addition, the rise in temperature of the designed inductor satisfies the temperature limit. The results show that the design methodology is feasible.

In future, the design method can be refined and expanded. The further developments are needed in the fringing flux and in the power loss calculations. The power loss and temperature rise tests would give a more realistic picture of the accuracy of the design. The next stage would be the compact design of a grid-side inductor of the LCL filter.

## References

- [1] P. Channegowda and V. John, "Filter optimization for grid interactive voltage source inverters," *IEEE Transactions on Industrial Electronics*, vol. 57, no. 12, pp. 4106–4114, Dec. 2010.
- [2] H. Karshenas and H. Saghafi, "Basic criteria in designing LCL filters for grid connected converters," in *IEEE International Symposium on Industrial Electronics*, vol. 3, July 2006, pp. 1996–2000.
- [3] Y. Jiao and F. Lee, "LCL filter design and inductor current ripple analysis for a three-level NPC grid interface converter," *IEEE Transactions on Power Electronics*, vol. 30, no. 9, pp. 4659–4668, Sept. 2015.
- [4] K. B. Park, F. Kieferndorf, U. Drottenik, S. Pettersson, and F. Canales, "Weight minimization of LCL filters for high power converters," in *9th International Conference on Power Electronics and ECCE Asia (ICPE-ECCE Asia)*, June 2015, pp. 142–149.
- [5] W. Wu, Y. He, and F. Blaabjerg, "An LLCL power filter for single-phase grid-tied inverter," *IEEE Transactions on Power Electronics*, vol. 27, no. 2, pp. 782–789, Feb. 2012.
- [6] R. Meyer and A. Mertens, "Design of LCL filters in consideration of parameter variations for grid-connected converters," in *IEEE Energy Conversion Congress and Exposition (ECCE)*, Sept. 2012, pp. 557–564.
- [7] "IEEE recommended practice and requirements for harmonic control in electric power systems," *IEEE Std 519-2014 (Revision of IEEE Std 519-1992)*, pp. 1–29, June 2014.
- [8] G. Zeng, T. Rasmussen, L. Ma, and R. Teodorescu, "Design and control of LCL-filter with active damping for active power filter," in *IEEE International Symposium on Industrial Electronics (ISIE)*, July 2010, pp. 2557–2562.
- [9] J. Muhlethaler, M. Schweizer, R. Blattmann, J. Kolar, and A. Ecklebe, "Optimal design of LCL harmonic filters for three-phase PFC rectifiers," *IEEE Transactions on Power Electronics*, vol. 28, no. 7, pp. 3114–3125, July 2013.
- [10] M. Liserre, F. Blaabjerg, and S. Hansen, "Design and control of an LCL-filter-based three-phase active rectifier," *IEEE Transactions on Industry Applications*, vol. 41, no. 5, pp. 1281–1291, Sept. 2005.
- [11] H. Nijende, N. Frohleke, and J. Bocker, "Optimized size design of integrated magnetic components using area product approach," in *European Conference on Power Electronics and Applications*, Sept. 2005, pp. 10 pp.–P.10.

- [12] W. Hurley, W. Wolfle, and J. Breslin, "Optimized transformer design: inclusive of high-frequency effects," *IEEE Transactions on Power Electronics*, vol. 13, no. 4, pp. 651–659, July 1998.
- [13] J. Biela, M. Schweizer, S. Waffler, and J. Kolar, "SiC versus Si-evaluation of potentials for performance improvement of inverter and dc-dc converter systems by SiC power semiconductors," *IEEE Transactions on Industrial Electronics*, vol. 58, no. 7, pp. 2872–2882, July 2011.
- [14] G. Grandi, M. Kazimierczuk, A. Massarini, U. Reggiani, and G. Sancinetto, "Model of laminated iron-core inductors for high frequencies," *IEEE Transactions on Magnetics*, vol. 40, no. 4, pp. 1839–1845, July 2004.
- [15] M. Bartoli, A. Reatti, and M. Kazimierczuk, "High-frequency models of ferrite core inductors," in *20th International Conference on Industrial Electronics, Control and Instrumentation*, vol. 3, Sept. 1994, pp. 1670–1675 vol.3.
- [16] ——, "Modelling iron-powder inductors at high frequencies," in *Conference Record of the IEEE Industry Applications Society Annual Meeting*, Oct. 1994, pp. 1225–1232 vol.2.
- [17] M. K. Kazimierczuk, *High-Frequency Magnetic Components (2nd Edition)*. Somerset, NJ, USA: John Wiley and Sons, 2013.
- [18] N. Ekekwe, K. White, and O. Ben, "Practical process in high frequency distribution transformer design," in *Conference on Electrical Insulation and Electrical Manufacturing and Coil Winding Technology*, Sept. 2003, pp. 121–128.
- [19] M. Rylko, B. Lyons, J. Hayes, and M. Egan, "Revised magnetics performance factors and experimental comparison of high-flux materials for high-current DC-DC inductors," *IEEE Transactions on Power Electronics*, vol. 26, no. 8, pp. 2112–2126, Aug. 2011.
- [20] M. Kazimierczuk and H. Sekiya, "Design of ac resonant inductors using area product method," in *IEEE Energy Conversion Congress and Exposition*, Sept. 2009, pp. 994–1001.
- [21] P. Wallmeier, "Pre-optimization of linear and nonlinear inductors using area-product formulation," in *Conference Record of the Industry Applications Conference (37th IAS Annual Meeting)*, vol. 4, Oct. 2002, pp. 2445–2450 vol.4.
- [22] H. Sekiya and M. K. Kazimierczuk, "Design of RF-choke inductors using core geometry coefficient," in *Proc. Electrical Manufacturing and Coil Winding Conf*, 2009.
- [23] J. Koppinen, F. M. Rahman, and M. Hinkkanen, "Effects of the switching frequency of a grid converter on the LCL filter design," in *IET International Conference on Power Electronics, Machines and Drives*, April 2016, in press.
- [24] J. Kukkola, M. Hinkkanen, and K. Zenger, "Observer-based state-space current controller for a grid converter equipped with an LCL filter: Analytical method

- for direct discrete-time design,” *IEEE Transactions on Industry Applications*, vol. 51, no. 5, pp. 4079–4090, Sept. 2015.
- [25] A. Rockhill, M. Liserre, R. Teodorescu, and P. Rodriguez, “Grid-filter design for a multimegawatt medium-voltage voltage-source inverter,” *IEEE Transactions on Industrial Electronics*, vol. 58, no. 4, pp. 1205–1217, April 2011.
  - [26] K. Jalili and S. Bernet, “Design of LCL filters of active-front-end two-level voltage-source converters,” *IEEE Transactions on Industrial Electronics*, vol. 56, no. 5, pp. 1674–1689, May 2009.
  - [27] A. V. d. Bossche and V. C. Valchev, *Inductors and Transformer for Power Electronics*. Boca Raton: Taylor and Francis, 2005.
  - [28] W. G. Hurley and W. H. Wölflé, *Transformers and inductors for power electronics : theory, design and applications (first edition)*. Somerset, NJ, USA: John Wiley and Sons, 2013.
  - [29] C. W. T. Mclyman, *Transformer and Inductor Design Handbook (3rd Edition, Revised and Expanded)*. New York, USA: Marcel Dekker, Inc, 2004.
  - [30] P. C. Sen, *Principles of Electric Machines and Power Electronics (second edition)*. NY, USA: John Wiley and Sons, 1996.
  - [31] M. Rylko, K. Hartnett, J. Hayes, and M. Egan, “Magnetic material selection for high power high frequency inductors in DC-DC converters,” in *Twenty-Fourth Annual IEEE Applied Power Electronics Conference and Exposition (APEC)*, Feb. 2009, pp. 2043–2049.
  - [32] G. Ortiz, J. Biela, and J. Kolar, “Optimized design of medium frequency transformers with high isolation requirements,” in *36th Annual Conference on IEEE Industrial Electronics Society (IECON)*, Nov. 2010, pp. 631–638.
  - [33] B. Lyons, J. Hayes, and M. Egan, “Design algorithm for high-current gapped foil-wound inductors in low-to-medium frequency DC-DC converters,” in *IEEE Power Electronics Specialists Conference (PESC)*, June 2007, pp. 1760–1766.
  - [34] ——, “Magnetic material comparisons for high-current inductors in low-medium frequency DC-DC converters,” in *Twenty Second Annual IEEE Applied Power Electronics Conference (APEC)*, Feb. 2007, pp. 71–77.
  - [35] Hellenic cables S.A., “Enamelled copper wires.” [Online]. Available: <http://www.etem.bg/products/en/229/brochures/copper-wires.PDF>
  - [36] P. Dowell, “Effects of eddy currents in transformer windings,” *Proceedings of the Institution of Electrical Engineers*, vol. 113, no. 8, pp. 1387–1394, Aug. 1966.
  - [37] J. Reinert, A. Brockmeyer, and R. De Doncker, “Calculation of losses in ferro and ferrimagnetic materials based on the modified Steinmetz equation,” *IEEE Transactions on Industry Applications*, vol. 37, no. 4, pp. 1055–1061, July 2001.

- [38] K. Venkatachalam, C. Sullivan, T. Abdallah, and H. Tacca, "Accurate prediction of ferrite core loss with nonsinusoidal waveforms using only Steinmetz parameters," in *IEEE Workshop on Computers in Power Electronics (COMPEL)*, June 2002, pp. 36–41.
- [39] J. Muhlethaler, J. Biela, J. Kolar, and A. Ecklebe, "Improved core-loss calculation for magnetic components employed in power electronic systems," *IEEE Transactions on Power Electronics*, vol. 27, no. 2, pp. 964–973, Feb. 2012.
- [40] R. Petkov, "Optimum design of a high-power, high-frequency transformer," *IEEE Transactions on Power Electronics*, vol. 11, no. 1, pp. 33–42, Jan. 1996.
- [41] Hitachi metals, "POWERLITE Inductor cores: Technical bulletin." [Online]. Available: [http://www.hilltech.com/pdf/Hitachi/Datasheets/POWERLITE\\_C-Cores\\_Technical\\_Bulletin.pdf](http://www.hilltech.com/pdf/Hitachi/Datasheets/POWERLITE_C-Cores_Technical_Bulletin.pdf)
- [42] JFE Steel Corporation, "Super Core: Electrical steel sheets for high-frequency application." [Online]. Available: <http://www.jfe-steel.co.jp/en/products/electrical/catalog/f1e-002.pdf>
- [43] *FRA5097 Frequency response Analyzer Instruction Manual*, NF Corporation, 6-3-20 Tsunashima higashi, Kohoku-ku, Yokohama 223-8508, 2006.

# Appendix

The MATLAB script of the design algorithm using the 2605SA1 core material under air-forced cooling condition is given below.

```
%////////// Forced Cooling_350 uH AMORPHOUS core ///////////////
clc;
close all;
clear all;
%% Constant-value define
mu_o = 4*pi*1e-7; % Permeability of air
mu_r = 5000; % Permeability of amorphous material
rho_w = 17.24e-9; % Electrical resistivity of copper wire
mu_rw = 1; % Winding relative permeability
fsw = 20e3; % Switching frequency

%% Specifications
L = 350e-6; % Inductance
Ipk = 28.12; % Peak current
Ipk_fun = 25.71; % Peak value of fundamental current
Ip_p_ripple = 4.67; % Peak-to-peak ripple current
Irms = 18.3; % Rms current
Ku = 0.4; % Window utilization factor
Jm_assum = 6; % Assumed current density (A/mm^2)
Bpk = 0.80*1.56; % Peak flux density

%% Initial Area product
Wm = (L*Ipk*Ipk)/2; % Energy of inductor
Ap_cal = ((2*Wm) / (Ku*Jm_assum*Bpk))*1000000; % Initail area product ...
    (mm^4)
floor (Ap_cal)

%% Winding specification
Aw_assum = Irms/Jm_assum; % Assumed area of copper wire (mm^2)
Aw = 3.142e-6; % Used Copper wire (m^2); din = 2.00 mm; dout = ...
    2.112 mm
dout = 2.112; % Nominal outer diameter (mm)
d = dout*1e-3; % Nominal outer diameter (m)
p = d; % Distance between two adjacent winding
Jm_cal = (Irms/Aw)/1000000; % Calculated current density (A/mm^2)

%% Final area product
Ap_cal_final = ((2*Wm) / (Ku*Jm_cal*Bpk))*1000000; % Final area ...
    product (mm^4)
floor (Ap_cal_final)

%% The final area product matches with the AMCC0010 core

%% Core specifications
A = 11e-3; % Core width
B = 13e-3; % Window width
C = 40e-3; % Window length
```

```

D = 20e-3; % Core height
lc = 150e-3; % Mean length of magnetic path
mass_core = 0.198 ; % Core mass (kg)
kc_core = 0.82; % Core fill factor

%% Calculation from core dimensions
Ac = A*D; % Core cross-section area (m^2)
Acore = A*D*1e6; % Core cross-section area (mm^2)
Ap_core = A*B*C*D*1e12; % Area product of the core (mm^4)
floor (Ap_core)
Wa = Ap_core/(Ac*1e6); % Window area (mm^2)
vol_core = lc*1e3*Ac*1e6; % Volume of core (mm^3)
floor (vol_core)
Nmax = ((Ku*Wa)/Aw)/1e6; % Maximum fitted winding

%% Number of turns calculation
N_cal = (L*Ipk)/(Bpk*Ac*kc_core)
N_final = 44; % Integer value of turn number

%% Air-gap calculation
u = 1; % Ratio of the effective width of the fringing flux ...
        % cross-section area to the air-gap length
k = 2; % Ratio of the effective magnetic path length of the ...
        % fringing flux to the air-gap length
lag = (((mu_o*Ac*N_final^2)/(2*L)) - (lc/(2*mu_r)))*1000 % Length ...
        % of air-gap without fringing flux (mm)
lg = lag*1e-3; % Iterative calculation between Ff and lag1
Ff = 1+(2*u*lg*(A+D+2*u*lg))/(k*A*D) % Fringing flux factor
lag1 = ...
        (((mu_o*Ac*Ff)/(2*L))*(N_final^2-(L*lc)/(mu_o*mu_r*Ac)))*1000 ...
        % Length of air-gap with fringing flux (mm)
Lf_required = ((mu_o*Ac*N_final^2)/((2*lg/Ff)+(lc/mu_r)))*1e6 % ...
        Required inductance (uH)

%% Calculation of fundamental and ripple component flux density (1)
Bpk1 = (L*Ipk_fun)/(N_final*Ac*kc_core);
Bpk_ripple = (L*Ip_p_ripple)/(2*N_final*Ac*kc_core);
Bpk_tot = Bpk1 + Bpk_ripple ;

%% Calculation of fundamental and ripple component flux density (2)
Bpk_1 = (Ipk_fun*Bpk)/Ipk; % Fundamental flux density
Bpk_ripple_1 = (Ip_p_ripple*Bpk)/(2*Ipk); % Ripple flux density
Bpk_tot_1 = Bpk_1 + Bpk_ripple_1; % Peak flux density

%% Winding length calculation
Ntl_1 = 15; % Number of turn at first layer
Ntl_2 = 7; % Number of turn at second layer
Bt = 2e-3; % Thickness of bobbin
lt_1 = (2*A*1e3) + (2*D*1e3) + (4*Bt*1e3); % Length of single turn ...
        % in first layer (mm)
lt_2 = (2*A*1e3) + (2*D*1e3) + (4*Bt*1e3) + (4*dout); % Length of ...
        % single turn in second layer (mm)
lw = 2*((Ntl_1*lt_1) + (Ntl_2*lt_2)); % Winding length (mm)
floor (lw)

```

```

%% Winding Loss calculation
Rwdc = (rho_w*lw)/(1000*Aw); % Dc resistance (ohm)
Pwdc = Irms^2*Rwdc; % Dc winding loss (Watt)
del_w = sqrt((rho_w)/(pi*mu_o*mu_rw*fsw)); % Skin depth of copper wire
Ao = (0.8343*(d^(1.5)))/((del_w)*p^(0.5)); % Dowell's constant
Nl = 1.5; % Number of layer
Fr1 = ...
    (exp(2*Ao)-exp(-(2*Ao))+2*sin(2*Ao))/(exp(2*Ao)+exp(-(2*Ao))-2*cos(2*Ao));
Fr2 = (exp(Ao)-exp(-Ao)-2*sin(Ao))/(exp(Ao)+exp(-Ao)+2*cos(Ao));
FR = Ao*(Fr1+(0.66*(Nl^2)-1)*Fr2); % AC-to-DC factor
Rwac = FR*Rwdc; % Ac resistance (ohm)
Pwac = FR*Pwdc; % Total winding loss (Watt)

%% CORE loss calculation
k = 6.5; % Steinmetz's parameter
alpha = 1.51; % Steinmetz's parameter
beta = 1.74; % Steinmetz's parameter
Pcore_sw = k*20^(alpha)*Bpk_ripple^(beta)*7.18; % Core loss density ...
    of 20 kHz (mW/cm^3) % 1 W/kg = 7.18 mW/cm^3
Vc = lc*Ac*1000000; % Core volume (cm^3)
Pc_sw = Pcore_sw*Vc; % Switching frequency core loss (mW)
Pcore_50 = k*0.05^(alpha)*Bpk^(beta)*7.18; % Core loss density of ...
    50 Hz (mW/cm^3)
Pc_50 = Pcore_50*Vc; % Fundamental core loss (mW)
Pcore_tot = Pc_50+Pc_sw; % Total core loss (mW)

%% Total loss calculation
Ptot = Pwac + Pcore_tot/1000; % Total inductor losses (Watt)

%% Total mass and volume claculation
Volume_winding = (lw/1000)*((pi*(dout*1e-3)^2)/4); % Volume (m^3)
mass_density_cu = 8920; % mass density of copper (kg/m^3)
mass_winding = mass_density_cu*Volume_winding*1000; % Mass of ...
    winding (g)
total_mass = mass_core*1000 + mass_winding; % Total mass (g)
volume_tot = (Volume_winding + Vc*1e-6)*1e9;
floor(volume_tot)

%% Thermal Modeling
%% Parameters define
v = 6.72; % Velocity of air (m/s)
f_silon = 0.8; % Emissivity of coil surface
f_silon1 = 0.95; % Emissivity of core surface
sigma = 5.67e-8; % Stephan-Boltzman constant
k_air = 0.031; % Thermal conductivity of air
k_core = 10; % Thermal conductivity of core

%% Length define
F = (A+C+A); % Vertical length of core
H = 34e-3; % Height of bobbin
H1 = A+A+D; % Open core length
H3 = F+D; % Total component length

```

```

%% Area define
lcf = 3e-3; % Air space between the coil and the core
Acf = 4*H*(A+2*Bt) + 4*H*(D+2*Bt); % Copper to core surface area
Aca = 4*H*(A+(2*Bt)+(2*d))+ 4*H*(D+(2*Bt)+(2*d)); % Copper to ...
    ambient surface area
Afa = 2*pi*A^2 + 4*B*A + 2*pi*A*D + 2*B*D; % Core open surface to ...
    ambient

%% Temperature and loss define
Tc = 293+77.5; % Copper Temperature including temp rise
    %Temperature rise should be equal to Del_T using Iterative ...
    process
Tf = Tc-1; % Core Temperature
Ta = 293; % Ambient temperature
Pc = 2.74; % Core loss
Pcu = 41.67; % Winding loss

%% Calculations
hc1 = (3.33+4.8*v^0.8)/(H^0.288); % Heat transfer coefficient (bobbin)
hc2 = (3.33+4.8*v^0.8)/(H1^0.288); % Heat transfer coefficient ...
    (open core)
hc3 = (3.33+4.8*v^0.8)/(H3^0.288); % Heat transfer coefficient ...
    (total component)

Rcf = 1/(((k_air*Acf)/lcf) + ...
    ((f_silon*sigma*Acf*(Tc^4-Tf^4))/(Tc-Tf)));
    % Winding to core thermal resistance
Rca = 1/((hc1*Aca)+((f_silon*sigma*Aca*(Tc^4-Ta^4))/(Tc-Ta)));
    % Winding to ambient thermal resistance
Rfa = 1/((hc2*Afa)+((f_silon1*sigma*Afa*(Tf^4-Ta^4))/(Tf-Ta)));
    % Core to ambient thermal resistance

%% Temperature rise
Del_T = ((Pcu*(Rcf+Rfa)+(Pc*Rfa))*Rca)/(Rcf+Rfa+Rca) % Temperature ...
    rise
Rth = Del_T/(Pcu+Pc); % Total thermal resistance

%% Heat transfer rate process
qd = (k_core*Ac*(Tc - Ta))/lc; % Conduction heat transfer rate
qr = 0.85*sigma*(Aca+Afa)*(Tc^4 - Ta^4); % Radiation heat transfer rate
qc = hc3*(Aca+Afa)*(Tc - Ta); % Convection heat transfer rate
q = qd+qr+qc; % Total heat transfer rate
Pt = Pc+Pcu; % Total loss (should be equal or less than heat ...
    transfer rate)
q1 = qd/q; % Percent of Conduction heat transfer rate
q2 = qr/q; % Percent of Radiation heat transfer rate
q3 = qc/q; % Percent of Convection heat transfer rate

```